JGR Solid Earth

RESEARCH ARTICLE
10.1029/2019JB017868

Finite Strain Analysis of Shear and Compressional Wave Velocities

Ariel Melinger-Cohen[1] and **Raymond Jeanloz**[1,2]

[1]Earth and Planetary Science, University of California, Berkeley, CA, USA, [2]Astronomy and Miller Institute for Basic Research in Science, University of California, Berkeley, CA, USA

Key Points:
- The spatial finite-strain formulation empirically fits high-pressure wave velocity measurements better than the material formulation
- A self-consistent finite-strain approach fits the data better than non-self-consistent approaches that have been widely used
- We extend the limited finite-strain analysis of the shearmodulus in previous work to improve discernment between finite strainapproaches

Correspondence to:
A. Melinger-Cohen,
azm892@berkeley.edu

Citation:
Melinger-Cohen, A., & Jeanloz, R. (2019). Finite Strain Analysis of Shear and Compressional Wave Velocities. *Journal of Geophysical Research: Solid Earth*, *124*, 11,651–11,677. https://doi.org/10.1029/2019JB017868

Received 17 APR 2019
Accepted 11 OCT 2019
Accepted article online 24 OCT 2019
Published online 20 NOV 2019

Abstract Published shear-modulus measurements for a wide variety of materials (Ar, Xe, H_2, He, NaCl, H_2O-VII, MgO, stishovite, bridgmanite) show that the Eulerian (spatial) description of energy vs. strain fits both finite- and infinitesimal-strain (e.g., wave velocity) elasticity data under high pressure. The Eulerian (spatial) formulations do so better than the Lagrangian (material) finite-strain description, with differences of 1% to 60% in both *P*- and *S*-wave velocities for these materials at the pressures of Earth's mantle. The results are significant in extending to shear previous findings that compressional (pressure-volume and bulk-modulus) measurements are also best fit using the spatial formulation. Our analysis empirically documents that a self-consistent Eulerian finite-strain equation of state offers a reliable means of describing the thermodynamic and elastic properties of planetary interiors.

1. Introduction

The equation of state, specifying volume (V) as a function of pressure (P) for crystals, fluids, and gases, plays a central role in planetary geophysics because it relates material elasticity to internal energy or free energy. In particular, the equation of state provides a thermodynamic basis for interpolating seismic wave velocities, which measure elastic response to infinitesimal strains, over the large volume strains experienced within planets. Consistency between infinitesimal- and finite-strain responses is an essential feature of planetary interior models since at least the work of Birch (1952).

Following Murnaghan's (1937) formulation, Birch (1947) developed a finite-strain equation of state grounded in continuum mechanics. Based on the spatial (Eulerian) frame of reference, it is applicable to condensed matter and is empirically found to reproduce infinitesimal- and finite-strain measurements of compressional properties such as volume and bulk modulus to high pressures. For example, ultrasonic (infinitesimal-strain) measurements of elastic wave velocities are found to be consistent with finite-strain static-compression (e.g., piston-cylinder and diamond-anvil cell) and shock wave measurements of the equation of state; such consistency for the compressional moduli is not found for other formulations, such as the material (Lagrangian) finite-strain or Murnaghan equations of state (Birch, 1978; Davies, 1973a; Jeanloz, 1989).

In the present work, we examine the consistency of equation-of-state formulations with measurements of the shear modulus under compression. Our motivation is twofold. First, variations in the seismological properties of Earth's interior are dominated by those in the shear modulus, the latter influencing both compressional- and shear wave velocity variations more than variations in the bulk modulus. It is important to extend to shear strains the earlier studies that were limited to compressional response. Second, numerous measurements of compressional and shear wave velocities under pressure have been published in recent years, based on Brillouin or impulsive light scattering, as well as high-frequency ultrasonics on samples taken to high pressures inside diamond-anvil cells. Therefore, we now have a large number of infinitesimal-strain wave-velocity measurements at large (finite-strain) volume compressions.

Our analysis builds on the papers of Jackson (1998) and Stixrude and Lithgow-Bertelloni (2005, 2010), who also pointed out that much of the published work uses a formulation of the elastic moduli that is not self-consistent with respect to a single description of the strain energy. We examine this concern about self-consistency in our analysis of both compressional- and shear wave velocities measured under pressure. Because the recent high-pressure measurements are all on dielectric samples, we do not consider metals here.

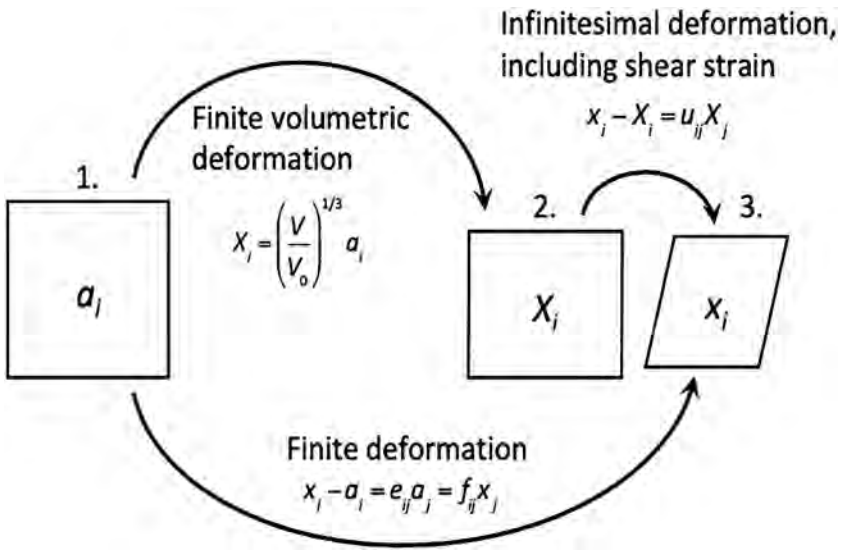

Figure 1. Schematic illustration of both infinitesimal and finite deformation of a material. (1) The original coordinates a_i of the material. (2) The material in its intermediate state X_i involving only volume compression. (3) The material in its final state x_i. Both X_i and x_i are deformed finitely from a_i, and infinitesimally from each other.

2. Derivation

We aim to derive a set of thermodynamically consistent formulas to describe the elastic moduli of solids as a function of finite strain. For the sake of clarity, and of consistency in terminology and concepts, we review the derivation of a thermodynamically consistent analysis describing the elastic moduli of solids as a function of finite strain (c.f., Davies, 1974; Stixrude & Lithgow-Bertelloni, 2005). The present summary is intended to (1) provide more details of the derivation, (2) explicitly develop the self-consistent formulation for both spatial and material frames, and (3) spell out the fourth-order terms. We consider materials that are hyperelastic, meaning that their properties are determined by a single, well-defined strain-energy function, so we ignore phase transformations and other nonelastic effects (e.g., fracture, anelastic, or plastic deformation). More significantly, we only consider finite volume strains; shear strains are taken to be infinitesimal because it is known that real materials respond to finite shear deformation through the creation and propagation of nonequilibrium defects such as dislocations.

We focus on the effects of finite strain on elastic properties and ignore thermal effects because these can be subsequently added in a self-consistent manner (e.g., Davies, 1973a; Wallace, 1972). Moreover, our presentation is simplified by assuming an isotropic polycrystalline aggregate and discussing only the isotropic bulk (K) and shear (G) moduli and corresponding compressional (V_P) and shear (V_S) wave velocities that are of predominant interest for seismology. Given this assumed isotropy, we take hydrostatic stress to depend uniquely on sample volume (and vice versa).

The finite-strain approach defines an initial configuration of zero strain, with each point in the material described by a position vector

$$a_i = (a_1, a_2, a_3) \tag{1}$$

and a final configuration following a finite deformation, denoted by the position vector

$$x_i = (x_1, x_2, x_3). \tag{2}$$

Using the Einstein summation convention, two displacement gradients (e_{ij}, f_{ij}) are defined (Thomsen,1972; Davies, 1974)

$$x_i - a_i = e_{ij} a_j = f_{ij} x_j \tag{3}$$

providing two deformation gradients, a material ("Lagrangian") gradient F_{ij} that references the initial state and a spatial ("Eulerian") gradient G_{ij} that references the final state (Figure 1):

$$F_{ij} = \frac{\partial x_i}{\partial a_j} = \delta_{ij} + e_{ij} \tag{4a}$$

$$G_{ij} = \frac{\partial a_i}{\partial x_j} = \delta_{ij} + f_{ij} \tag{4b}$$

Whereas the material description tracks individual particles (e.g., atoms) in the deforming medium, the spatial description employs the laboratory frame of reference, with the deformed positions x_i measured using the same ruler as the original points a_i.

Because shear (nonvolumetric or deviatoric) strains must be treated infinitesimally, we follow Thurston (1965), Thomsen (1972), and Davies (1974) in identifying an intermediate configuration that encompasses all of the final state's finite volume deformation (Figure 1):

$$X_i = (X_1, X_2, X_3). \tag{5}$$

The infinitesimal displacement gradients u_{ij} relate to the intermediate deformation state, and v_{ij} to the final deformed state. They are both referred to in the final state (x_i) only.

$$u_i = x_i - X_i \tag{6a}$$

$$x_i - X_i = u_{ij} X_j \tag{6b}$$

$$x_i - X_i = v_{ij} x_j. \tag{6c}$$

The final state x_i is derived by infinitesimally straining the intermediate state X_i. The shear component arises entirely between these two states; (6b) and (6c) are both in a spatial (Eulerian) reference frame. However, these provide alternative descriptions of the infinitesimal deformation that puts all of the shear strain in the final state. Specifically, v_{ij} and u_{ij} are infinitesimal gradients in terms of coordinates that respectively do and do not contain the shear strains.

From the displacement gradients, we define the following strain tensors, the first two of which (respectively, material and spatial tensors) refer to a finite deformation that includes both volumetric and shear strain.

$$\eta_{ij} = \frac{1}{2}\left(e_{ij} + e_{ji} + e_{ki}e_{kj}\right) = \frac{1}{2}\left(\frac{\partial x_k}{\partial a_i}\frac{\partial x_k}{\partial a_j} - \delta_{ij}\right) \tag{7a}$$

$$E_{ij} = \frac{1}{2}\left(f_{ij} + f_{ji} - f_{ik}f_{jk}\right) = \frac{1}{2}\left(\delta_{ij} - \frac{\partial a_i}{\partial x_k}\frac{\partial a_j}{\partial x_k}\right). \tag{7b}$$

The third and fourth displacement gradients refer to the infinitesimal components of the deformation and encompass all of the shear strain.

$$R_{ij} = \frac{1}{2}\left(u_{ij} + u_{ji} + u_{ki}u_{kj}\right) = \frac{1}{2}\left(\frac{\partial x_k}{\partial X_i}\frac{\partial x_k}{\partial X_j} - \delta_{ij}\right) \tag{7c}$$

$$S_{ij} = \frac{1}{2}\left(v_{ij} + v_{ji} - v_{ik}v_{jk}\right) = \frac{1}{2}\left(\delta_{ij} - \frac{\partial X_i}{\partial x_k}\frac{\partial X_j}{\partial x_k}\right). \tag{7d}$$

Note that in formulating the spatial tensors, we adopt the frame-indifferent tensors utilized by Thomsen (1972) and Davies (1973b). This leads to a definition of the spatial tensor that differs from the Almansi-Hamel strain tensor that Murnaghan (1937), Birch (1947), and Thurston (1965) used, which is not frame indifferent. The difference is seen in the definitions of the spatial strain tensor E_{ij}, in which our definition keeps the indices constant in x_i, whereas the non-frame-indifferent version keeps indices constant in a_i (i.e., $E_{ij})_{Birch} = \frac{1}{2}\left(\delta_{ij} - \frac{\partial a_k}{\partial x_i}\frac{\partial a_k}{\partial x_j}\right)$ (Birch, 1947). This difference carries over into the associated strain tensor S_{ij}.

The Cauchy stress tensor (T_{ij}) and effective elastic moduli (c_{ijkl}) under hydrostatic stress (i.e., volume compression) are (Thurston, 1965)

$$T_{ij} = \rho\left(\frac{\partial U}{\partial R_{ij}}\right)_S = \rho\left(\frac{\partial U}{\partial S_{ij}}\right)_S \tag{8}$$

$$c_{ijkl} = \frac{\partial T_{ij}}{\partial R_{kl}} = \rho\left(\frac{\partial^2 U}{\partial R_{ij}\partial R_{kl}}\right)_S + P\delta_{ij}\delta_{kl} \tag{9a}$$

$$c_{ijkl} = \frac{\partial T_{ij}}{\partial S_{kl}} = \rho\left(\frac{\partial^2 U}{\partial S_{ij}\partial S_{kl}}\right)_S + P\delta_{ij}\delta_{kl} \tag{9b}$$

where ρ is mass density, P is pressure, V is specific volume, and only the diagonal elements of R_{ij} and S_{ij} yield a change in density ($\rho = 1/V$):

$$\frac{\partial \rho}{\partial R_{kl}} = \frac{\partial \rho}{\partial S_{kl}} = -\rho\delta_{kl} \tag{10}$$

As R_{ij} and S_{ij} are spatial (Eulerian), so is the Cauchy stress tensor and is distinct from material and mixed stress tensors (e.g., first and second Piola-Kirchoff stress tensors: Weiner, 2002).

Here and throughout our derivation, we define the stress tensor and elastic moduli through the internal energy, U, relevant to isentropic compression and moduli associated with wave propagation, as used in seismology. However, equivalent expressions can be found for isothermal compression and moduli through the Helmholtz free energy (e.g., Wallace, 1972).

The elastic moduli expressed in (9) refer to an infinitesimal displacement through S_{ij}, thereby accounting for shear deformation (Thurston, 1965). However, in order to reconcile the possible presence of nonvolumetric strain with the hyperelastic assumption that all deformation is reversible, we must express the stress and elastic moduli in terms of a finite deformation. Thus, we translate between the prestressed infinitesimal strain tensor S_{ij} and the finite strain tensors η_{kl} and E_{kl} that include both volumetric and nonvolumetric strain. We start by writing the stress tensor

$$T_{ij} = \rho\left(\frac{\partial U}{\partial R_{ij}}\right) = \rho\left(\frac{\partial U}{\partial \eta_{kl}}\right)\left(\frac{\partial \eta_{kl}}{\partial R_{ij}}\right) \tag{11a}$$

$$T_{ij} = \rho\left(\frac{\partial U}{\partial S_{ij}}\right) = \rho\left(\frac{\partial U}{\partial E_{kl}}\right)\left(\frac{\partial E_{kl}}{\partial S_{ij}}\right) \tag{11b}$$

and evaluate the strain-strain derivatives $\left(\frac{\partial \eta_{kl}}{\partial R_{ij}}\right)$ and $\left(\frac{\partial E_{kl}}{\partial S_{ij}}\right)$ to obtain the deformation gradients at $x_i = X_i$ (Stixrude & Lithgow-Bertelloni, 2005):

$$\begin{aligned}\left(\frac{\partial \eta_{kl}}{\partial R_{ij}}\right) &= \frac{\partial}{\partial R_{ij}}\left(\frac{1}{2}\frac{\partial x_s}{\partial a_k}\frac{\partial x_s}{\partial a_l}\right) = \frac{\partial}{\partial R_{ij}}\left(\frac{1}{2}\frac{\partial x_s}{\partial X_p}\frac{\partial X_p}{\partial a_k}\frac{\partial x_s}{\partial X_q}\frac{\partial X_q}{\partial a_l}\right) = \frac{\partial}{\partial R_{ij}}\left(\frac{1}{2}\frac{\partial x_s}{\partial X_p}\frac{\partial x_s}{\partial X_q}\frac{\partial X_p}{\partial a_k}\frac{\partial X_q}{\partial a_l}\right)\\ &= \frac{\partial}{\partial R_{ij}}\left(\left(R_{pq} + \frac{1}{2}\delta_{pq}\right)\frac{\partial X_p}{\partial a_k}\frac{\partial X_q}{\partial a_l}\right) = \left(\delta_{ip}\delta_{jq}\frac{\partial X_p}{\partial a_k}\frac{\partial X_q}{\partial a_l}\right) = \frac{\partial X_i}{\partial a_k}\frac{\partial X_j}{\partial a_l} = F_{ik}F_{jl}\end{aligned} \tag{12a}$$

$$\begin{aligned}\left(\frac{\partial E_{kl}}{\partial S_{ij}}\right) &= \frac{\partial}{\partial S_{ij}}\left(\frac{1}{2}\frac{\partial a_k}{\partial x_s}\frac{\partial a_l}{\partial x_s}\right) = \frac{\partial}{\partial S_{ij}}\left(\frac{1}{2}\frac{\partial a_k}{\partial X_p}\frac{\partial X_p}{\partial x_s}\frac{\partial a_l}{\partial X_q}\frac{\partial X_q}{\partial x_s}\right) = \frac{\partial}{\partial S_{ij}}\left(\frac{1}{2}\frac{\partial X_p}{\partial x_s}\frac{\partial X_q}{\partial x_s}\frac{\partial a_k}{\partial X_p}\frac{\partial a_l}{\partial X_q}\right)\\ &= \frac{\partial}{\partial S_{ij}}\left(\left(S_{pq} - \frac{1}{2}\delta_{pq}\right)\frac{\partial a_k}{\partial X_p}\frac{\partial a_l}{\partial X_q}\right) = \left(\delta_{ip}\delta_{jq}\frac{\partial a_k}{\partial X_p}\frac{\partial a_l}{\partial X_q}\right) = \frac{\partial a_k}{\partial X_i}\frac{\partial a_l}{\partial X_j} = G_{ki}G_{lj.}\end{aligned} \tag{12b}$$

This effectively brings all shear (deviatoric, nonvolumetric) strains into the infinitesimal displacements, ensuring that all finite-strain components are completely volumetric so as to avoid irreversible deformations. Thus, T_{ij} and c_{ijkl} can be rewritten in terms of either E_{mn} or η_{mn}:

$$T_{ij} = \rho F_{im}\left(\frac{\partial U}{\partial \eta_{mn}}\right)F_{jn} = \rho G_{mi}\left(\frac{\partial U}{\partial E_{mn}}\right)G_{nj} \tag{13}$$

$$c_{ijkl} = \rho F_{im}F_{kp}\left(\frac{\partial^2 U}{\partial \eta_{mn}\partial \eta_{pq}}\right)F_{jn}F_{lq} - P\delta_{ij}^{kl} = \rho G_{mi}G_{pk}\left(\frac{\partial^2 U}{\partial E_{mn}\partial E_{pq}}\right)G_{nj}G_{ql} - P\Delta_{ij}^{kl} \tag{14}$$

where

Table 1
Concise Third-Order Expressions for Pressure, Bulk Modulus, and Elastic Modulus[a]

	Expression
Pressure (P)	$\left(\frac{1}{3}\right)f_n(1+nf_n)^{\frac{3+n}{n}}\left(a+\frac{bf_n}{2}\right)$
Bulk modulus (K)	$\left(\frac{1}{18}\right)(1+nf_n)^{\frac{3+n}{n}}\left(2a+[2b+a(6+4n)]f_n+3b[1+n]{f_n}^2\right)$
Elastic modulus (c_{ijkl})	$(1+nf_n)^{\frac{8+3n}{4}}(A+Bf_n)-\frac{1}{3}(1+nf_n)^{\frac{3+n}{n}}\left(af_n+\frac{b{f_n}^2}{2}\right)\zeta_{kl}^{ij}$
a	$9K_0$
b	$-27K_0\left(2+n-K_0^{'}\right)$
A	c_{ijkl0}
B	$\frac{1}{2}\left[6K_0\left(\delta_{ijkl}+c_{ijkl0}^{'}\right)-c_{ijkl0}(8+3n)\right]$

[a]Expressions are generalized between material ($n=-2$) and spatial ($n=2$) reference frames. Parameters a, b, A, and B represent the coefficients in the respective Taylor series. Subscript *0* refers to ambient conditions.

$$\delta_{ij}^{kl}=\delta_{ik}\delta_{jl}+\delta_{il}\delta_{jk}-\delta_{ij}\delta_{kl} \tag{15a}$$

$$\Delta_{ij}^{kl}=-\delta_{ik}\delta_{jl}-\delta_{il}\delta_{jk}-\delta_{ij}\delta_{kl} \tag{15b}$$

for material and spatial reference frames, respectively.

Specializing from here on to the case of cubic symmetry, a hydrostatic stress produces an isotropic strain, and the strain tensors take the form corresponding to pure dilatational strain.

$$\eta=\frac{1}{2}\left[\left(\frac{\rho}{\rho_0}\right)^{\frac{-2}{3}}-1\right] \tag{16a}$$

$$E=\frac{1}{2}\left[1-\left(\frac{\rho}{\rho_0}\right)^{\frac{2}{3}}\right]. \tag{16b}$$

Under this condition, the crystal has an interatomic spacing of equal length along the three principle axes, which undergo only bulk, volumetric strain. The deformation gradients accordingly become diagonal. This simplification allows us to associate isotropic strains with isotropic stress (hydrostatic pressure) exerted on an isotropic polycrystalline sample, as discussed below. For high-pressure applications, it is useful to define strain as positive upon compression rather than expansion, so we use the generalized strain tensor f_n:

$$f_n=\frac{1}{n}\left[\left(\frac{\rho}{\rho_0}\right)^{\frac{n}{3}}-1\right], \tag{17}$$

with $n=2$ and -2 for spatial and material frames, to define

$$\eta_{ij}=-f_{-2}\delta_{ij}\ and\ f_{-2}=\frac{1}{2}\left[1-\left(\frac{\rho}{\rho_0}\right)^{\frac{-2}{3}}\right] \tag{18a}$$

$$E_{ij}=-f_2\delta_{ij}\ and\ f_2=\frac{1}{2}\left[\left(\frac{\rho}{\rho_0}\right)^{\frac{2}{3}}-1\right] \tag{18b}$$

(Jeanloz, 1989).

Because $\frac{\partial f_n}{\partial E_{ij}}=\frac{\partial f_n}{\partial \eta_{ij}}=-1$, the elastic moduli are rewritten as

$$c_{ijkl}=\rho_0\left(\frac{\rho_0}{\rho}\right)^{\frac{1}{3}}\left(\frac{\partial^2 U}{\partial {f_{-2}}^2}\right)\delta_{im}\delta_{jn}\delta_{kp}\delta_{lq}-P\delta_{ij}^{kl}=\rho_0\left(\frac{\rho}{\rho_0}\right)^{\frac{7}{3}}\left(\frac{\partial^2 U}{\partial {f_2}^2}\right)\delta_{mi}\delta_{nj}\delta_{pk}\delta_{ql}-P\Delta_{ij}^{kl}, \tag{19}$$

and then

Table 2
Explicit Third-Order Expressions for Pressure, Elastic Modulus, Bulk Modulus, and Shear Modulus[a]

	Spatial	Material
Pressure (P)	$K_0 f_2(1+2f_2)^{\frac{5}{2}}\left(3+\frac{-9(4-K_0')}{2}f_2\right)$	$K_0 f_{-2}(1-2f_{-2})^{\frac{-1}{2}}\left(3-\frac{9K_0'}{2}f_{-2}\right)$
Elastic modulus (c_{ijkl})	$(1+2f_2)^{\frac{5}{2}}\left(c_{ijkl0}+\left[3K_0c'_{ijkl0}-5c_{ijkl0}\right]f_2+\left[\Delta_{ijkl}K_0\left(24-\frac{9}{2}K_0'\right)-14c_{ijkl0}+6K_0c'_{ijkl0}\right]f_2^{\,2}\right)$	$(1-2f_{-2})^{\frac{-1}{2}}\left(c_{ijkl0}+\left[3K_0c'_{ijkl0}-c_{ijkl0}\right]f_{-2}-\frac{9K_0K_0'}{2}f_{-2}^{\,2}\delta_{ijkl}\right)$
Bulk modulus (K)	$K_0(1+2f_2)^{\frac{5}{2}}\left(1+\left[3K_0'-5\right]f_2+\frac{27}{2}(K_0'-4)f_2^{\,2}\right)$	$K_0(1-2f_{-2})^{\frac{-1}{2}}\left(1+\left[3K_0'-1\right]f_{-2}-\frac{9}{2}K_0'f_{-2}^{\,2}\right)$
Shear modulus (G)	$(1+2f_2)^{\frac{5}{2}}\left(G_0+\left[3K_0G_0'-5G_0\right]f_2+\left[K_0\left(\frac{9}{2}K_0'-24+6G_0'\right)-14G_0\right]f_2^{\,2}\right)$	$(1-2f_{-2})^{\frac{-1}{2}}\left(G_0+(3K_0G_0'-G_0)f_{-2}-\left[2G_0+K_0\left(6+6G_0'+\frac{9}{2}K_0'\right)\right]f_{-2}^{\,2}\right)$

[a]Expressions are written out explicitly in both spatial and material reference frames. Expressions for K and G that are generalized using the parameter n are not currently attainable. Both spatial formulations agree with those reported in Stixrude and Lithgow-Bertelloni (2005). Subscript 0 refers to ambient conditions.

$$c_{ijkl}=\rho_0\left(\frac{\rho}{\rho_0}\right)^{\frac{n(8+3n)}{12}}\left(\frac{\partial^2 U}{\partial {f_n}^2}\right)\delta_{im}\delta_{jn}\delta_{kp}\delta_{lq}-P\zeta_{ij}^{kl} \tag{20a}$$

where

$$\zeta_{ij}^{kl}=\frac{-n}{2}\left(\delta_{ik}\delta_{jl}+\delta_{il}\delta_{jk}\right)-\delta_{ij}\delta_{kl}. \tag{20b}$$

In order to express the isentropic elastic moduli as a function of strain (neglecting temperature), the internal energy is expanded as a Taylor series using the finite-strain tensor f_n:

$$\rho_0 U=\rho_0 U_0+\frac{1}{2}a_{ijk}{f_n}^2+\frac{1}{6}a_{ijklmn}{f_n}^3+\frac{1}{24}a_{ijklmnop}{f_n}^4+.... \tag{21}$$

An expression for pressure is derived by $P=-\left(\frac{\partial U}{\partial V}\right)_S$: in this case, the strain is isotropic, and the subscripts of the coefficients reflect isotropic symmetry:

$$P=\frac{1}{3}(1+nf_n)^{\frac{3+n}{n}}\left(a_{iikk}f_n+\frac{1}{2}a_{iikkmm}{f_n}^2+\frac{1}{6}a_{iikkmmoo}{f_n}^3+...\right). \tag{22}$$

An expression for the elastic modulus is obtained from (21) and (22):

$$c_{ijkl}=(1+nf_n)^{\frac{(8+3n)}{4}}\left(a_{ijkl}+\frac{1}{2}a_{ijklmn}f_n+\frac{1}{6}a_{ijklmnop}{f_n}^2+...\right)-P\zeta_{ij}^{kl}. \tag{23}$$

P in (23) is the same as in (22). As written, (22) and (23) are expanded to fourth order in strain in the energy function given in (21). In principle, higher-order terms are possible, but experimental data are at present inadequate for determining the additional coefficients (i.e., higher-order elastic constants that are typically resolved by measurements). The coefficients in (22) and (23) are evaluated by taking the pressure derivatives and evaluating at initial conditions (zero strain). Values are listed in Tables 1–4.

Assuming an isotropic polycrystal of cubic minerals, the Voigt and Reuss bounds become equivalent (Hill, 1952), and the isentropic bulk and shear moduli are found from (23) using the following expressions for isotropic materials (in the abbreviated Voigt matrix form):

$$K_S=\frac{c_{ijkl}\delta_{ij}\delta_{kl}}{3}=\frac{C_{11}+2C_{12}}{3} \tag{24}$$

$$G=C_{44}=\frac{C_{11}-C_{12}}{2}. \tag{25}$$

At this point, the moduli must be evaluated separately for spatial and material reference frames, yielding the expressions in Tables 1–4. The bulk modulus expressions are alternatively reproduced through the pressure expression, where $K_S=-V\left(\frac{\partial P}{\partial V}\right)_S$. The third-order spatial terms match the expressions given by Stixrude and Lithgow-Bertelloni (2005).

The longitudinal (compressional) and transverse (shear) sound velocities in an isotropic medium are related to its bulk and shear moduli through

$${V_P}^2=\left(K_S+\frac{4}{3}G\right)/\rho \tag{26a}$$

$${V_S}^2=G/\rho \tag{26b}$$

showing that variations in G dominate variations in both V_P and V_S relative to those in K_S.

For cubic crystals, the bulk modulus is the same as that of the single crystal, but there are two shear moduli, and these must be combined to obtain the isotropic average. The shear

Table 3
Concise Fourth-Order Expressions for the Pressure, Bulk Modulus, and Elastic Modulus[a]

	General
Pressure (P)	$\frac{1}{3}f_n(1+nf_n)^{\frac{3+n}{n}}\left(a+\frac{b}{2}f_n+\frac{c}{6}{f_n}^2\right)$
Bulk modulus (K)	$\frac{1}{54}(1+nf_n)^{\frac{3+n}{n}}(6a+[6b+6a(3+2n)]f_n+[3c+9b(1+n)]{f_n}^2+c[3+4n]{f_n}^3)$
Elastic modulus (c_{ijkl})	$(1+nf_n)^{\frac{8+3n}{4}}\left(A+Bf_n+\frac{C}{2}{f_n}^2\right)-\frac{1}{3}f_n(1+nf_n)^{\frac{3+n}{n}}\left(a+\frac{b}{2}f_n+\frac{c}{6}{f_n}^2\right)\zeta^{ij}_{kl}$
a	$9K_0$
b	$-27K_0\left(2+n-K_0'\right)$
c	$9K_0\left[27+n(36+11n)-K_0'(27-18n)+9\left({K_0}^2+K_0K_0''\right)\right]$
A	c_{ijkl0}
B	$\frac{1}{4}\left[12K_0\left(\zeta^{ij}_{kl}+c'_{ijkl0}\right)-(9n+2n^2)c_{ijkl0}\right]$

[a]Expressions are generalized between material and spatial reference frames using the parameter n. Parameters a, b, A, and B represent the coefficients in the respective Taylor series. Subscript 0 refers to ambient conditions.

wave velocity is averaged in a similar way and is related to the shear modulus through the elastic moduli:

$$\rho {V_{S1}}^2 = c_{44} \tag{27a}$$

$$\rho {V_{S1}}^2 = \frac{c_{11}-c_{12}}{2}. \tag{27b}$$

The Voigt average considers strain to be uniform throughout the aggregate,

$$5G_V = 3c_{44} + (c_{11}-c_{12}), \tag{28}$$

and the Reuss average takes stress to be uniform throughout the aggregate,

$$5/G_R = \frac{3}{c_{44}} + \frac{4}{(c_{11}-c_{12})} \tag{29}$$

These formulas represent upper (Voigt) and lower (Reuss) bounds for the average value of G, and the arithmetic mean of the two is commonly taken as the Voigt-Reuss-Hill (VRH) average (Hill, 1952). We adopt the VRH mean, which provides a compromise between the endmember Voigt and Reuss averages.

The elasticity equations derived here use the self-consistent approach of Stixrude and Lithgow-Bertelloni (2005), which truncates the Taylor expansion (21) of internal energy at a given power of strain and then combines derivatives within this approximation to determine pressure and elastic moduli, c_{ijkl}. At third order in the energy expansion, for example, this results in the first term in (23) extending to the second power of f_2 and the pressure contribution (second term) contributing to the elastic moduli only to the first power in f_2.

In contrast, Davies and Dziewonski (1975) present a non-self-consistent formulation in which the two terms in (23) are extended to the same power of f_2, thereby truncating the order of the first term by one power. Thus, the third-order, non-self-consistent spatial equations for bulk and shear moduli expand only to the first power in f_2:

$$K = (1+2f_2)^{5/2}(K_0 + K_0(-5+3K_0')f_2) \tag{30a}$$

$$G = (1+2f_2)^{5/2}(G_0 + (-5G_0 + 3K_0G_0')f_2), \tag{30b}$$

whereas the self-consistent equations derived here include an additional term:

$$K = (1+2f_2)^{5/2}\left(K_0 + K_0(-5+3K_0')f_2 + \frac{27}{2}K_0\left(K_0'-4\right){f_2}^2\right) \tag{31a}$$

$$G = (1+2f_2)^{5/2}\left(G_0 + (-5G_0 + 3K_0G_0')f_2 + \left(-24K_0-14G_0 + \frac{9K_0K_0'}{2} + 6K_0G_0'\right){f_2}^2\right). \tag{31b}$$

Because Davies and Dziewonski's (1975) formulation has been used in numerous geophysical studies, we examine the degree to which it matters whether or not the self-consistent approach is followed.

Table 4
Explicit Fourth-Order Expressions for Pressure, Elastic Modulus, Bulk Modulus, and Shear Modulus[a]

	Spatial	Material
Pressure (P)	$K_0 f_2(1+2f)^{\frac{5}{2}}\left(3+\frac{9}{2}[4-K_0']f_2+\frac{1}{2}[143-(63+9K_0')K_0'+9K_0K_0'']f_2^{\ 2}\right)$	$K_0 f_{-2}(1-2f_{-2})^{\frac{7}{2}}\left(3+\frac{9}{2}K_0'f_{-2}+\frac{1}{2}[9K_0'(1+K_0')+9K_0K_0''-1]f_{-2}^{\ 2}\right)$
Elastic Modulus (c_{ijkl})	$(1+2f_2)^{\frac{5}{2}}\left(c_{ijkl0}+[3K_0c_{ijkl0}'-5c_{ijkl0}]f_2+\frac{1}{2}\left[35c_{ijkl0}-(36+9K_0')K_0'c_{ijkl0}\right.\right.$ $\left.\left.+9K_0^{\ 2}c_{ijkl0}''\right]f_2^{\ 2}+\frac{1}{2}[126c_{ijkl0}-(239+81K_0'-9K_0'^2-9K_0'')K_0\Lambda_{ijkl}$ $+18K_0\left(K_0'c_{ijkl0}+K_0c_{ijkl0}''-\frac{16}{3}c_{ijkl0}'\right)]f_2^{\ 3}\right)$	$(1-2f_{-2})^{\frac{7}{2}}\left(c_{ijkl0}+[3K_0c_{ijkl0}'-c_{ijkl0}]f_{-2}+\frac{1}{2}\left[9K_0\left(K_0'c_{ijkl0}+K_0c_{ijkl0}''\right)\right.\right.$ $\left.\left.-c_{ijkl0}]f_{-2}^{\ 2}+\frac{1}{2}\left[9K_0\delta_{ijkl}\left(K_0'-K_0'^2-K_0''-\frac{23}{9}\right)-18K_0^{\ 2}c_{ijkl0}''\right.\right.$ $\left.\left.-6c_{ijkl0}-K_0c_{ijkl0}'(24\right.$ $\left.+18K_0'\right)]f_{-2}^{\ 3}\right)$
Bulk Modulus (K)	$K_0(1+2f_2)^{\frac{5}{2}}\left(1+[3K_0'-5]f_2+\frac{1}{2}[35-9K_0(4-K_0'-K_0')]f_2^{\ 2}\right.$ $\left.+\frac{1}{2}\left[\frac{817}{3}-231K_0'+33K_0'^2+33K_0K_0'\right]f_2^{\ 3}\right)$	$K_0(1-2f_{-2})^{\frac{7}{2}}\left(1+[3K_0'-1]f_{-2}+\frac{1}{2}[9K_0'^2+9K_0K_0''-1]f_{-2}^{\ 2}\right.$ $\left.+\frac{1}{2}\left[\frac{5}{3}-15K_0'-15K_0'^2-15K_0K_0''\right]f_{-2}^{\ 3}\right)$
Shear Modulus (G)	$(1+2f_2)^{\frac{5}{2}}\left(G_0+[3K_0G_0'-5G_0]f_2+\frac{1}{2}[35G_0-9K_0G_0'(4-K_0')+9K_0^2G_0'']f_2^{\ 2}\right.$ $\left.+\frac{1}{2}[239K_0+126G_0+9K_0K_0'(K_0'-9)+K_0G_0'(18K_0'-96)\right.$ $\left.+9K_0^{\ 2}(K_0'^2+2G_0')]f_2^{\ 3}\right)$	$(1-2f_{-2})^{\frac{7}{2}}\left(G_0+[3K_0G_0'-G_0]f_{-2}+\frac{1}{2}[9K_0K_0'G_0'+9K_0^2G_0'']f_{-2}^{\ 2}\right.$ $\left.-G_0]f_{-2}^{\ 2}-\frac{1}{2}[23K_0+6G_0+9K_0K_0'(3+K_0')+24K_0G_0'\right.$ $\left.+18K_0K_0'G_0'+9K_0^2K_0'+18K_0^2G_0'^2]f_{-2}^{\ 3}\right)$

[a]Expressions are written out explicitly in both spatial and material reference frames. Expressions for K and G that are generalized using the parameter n are not currently attainable. The spatial bulk modulus agrees with that reported in Jeanloz (1989). Subscript 0 refers to ambient conditions.

3. Analysis

3.1. Results

We use the third-order equations derived above to assess the applicability of the two most commonly used reference frames, spatial ($n = 2$, Eulerian) and material ($n = -2$, Lagrangian). We did not use the fourth-order equations, because sufficient laboratory data are not yet available. For each material considered, we check whether the values and derivatives collected over a large range of compression are consistent with high-precision measurements at low compressions. To do this, we compare the extrapolation of a low-pressure data set to high compressions with independent measurements at high compressions. Occasionally, we have too few data to make this independent comparison and instead determine the internal consistency of a single set of measurements.

We use published experimental data to supply the reference material properties (Table 5), allowing us to calculate the adiabatic bulk modulus, shear modulus, and sound velocities (V_P and V_S) for 9 materials over a range of pressures. These include some lower symmetry materials, such as perovskite-structured $MgSiO_3$ and rutile-structured SiO_2 stishovite. The isotropic formulation summarized here is a simplification, but the results appear to be equally robust for lower-symmetry as for cubic crystals. Pressures are calculated as an isothermal function of density, using the same elastic moduli as for the velocities but now converted from isentropic to isothermal values. Errors are propagated to generate uncertainty envelopes around the calculated curves. In order to test the finite-strain formulations, we examine materials covering a wide range of bulk and shear modulus values. For most materials, the elastic constants were published in the literature, but in some cases we fit the data to extract the constants using the self-consistent spatial formulations (Table 2). For some materials, data from multiple studies had to be combined, as detailed in Table 5.

The calculated moduli and velocities are then compared with a wider collection of experimental data and a few predictions from theory (Figures 2–10). We compare self-consistent and non-self-consistent formulas (30) and (31) in the same manner. The data include elasticity measurements from Brillouin spectroscopy and ultrasonic interferometry, and the theoretical predictions are derived from density functional theory.

To quantify the misfit in each comparison, we give the average percent deviation (*% Dev*) in absolute value and the root-mean-square deviation (*RMSrD*) of the calculated moduli and velocities relative to the data:

Table 5
Elastic and Thermodynamic Material Constants[a]

	ρ_0 (g/cm^3)	P_0 (GPa)	K_{0S} (GPa)	K_{0S}'	G_0 (GPa)	G_0'	α_0 (10^{-5}/K)	γ_0	$\alpha_0{*}\gamma_0{*}T$
MgO[1]	3.585	0	163.20 (10)	3.83 (15)	130.20 (10)	2.21 (10)	3.12	1.52 (3)	0.014
$MgSiO_3$[2]	4.106	0	252.0 (2)	4.4 (1)	172.0 (1)	2.00 (1)	2.2	1.54 (9)	0.010
NaCl[3]	2.164	0	26.26 (13)	4.27 (1.4)	14.22 (1)	1.52 (1)	11.70	1.52	0.053
SiO_2 (stishovite)[4]	4.287	0	308 (1)	4.0 (1)	228 (1)	1.1 (1)	1.64	1.35	0.007
H_2O-VII[5]	1.687	0	24.67 (93)	4.03 (7)	12.70 (6.5)	2.38 (9)	11.39	1.2 (1)	0.041
Ar[6]	2.553	4.3	26.56 (23)	4.63 (24)	5.8 (9)	1.45 (12)	0.24	1.95	0.140
Xe[7]	3.971	0.43	5.83 (12)	5.94 (10)	1.87 (4)	2.17 (6)	0.27	2.26	0.180
H_2[8]	0.264	6.4	21.1 (2)	3.26 (2)	6.8 (2)	1.51 (2.5)	23.90	1.81	0.130
He[9]	0.9881	13	39.1 (2.4)	3.41 (2)	13.7 (1.5)	1.63 (1.5)	20.40	1.61	0.099

[a]Material constants are taken from the literature, or when not provided, fitted from data in the literature. When known, errors in last digits are shown in parentheses after the values. [1]Values are from Sinogeikin and Bass (2000). α_0 is from Suzuki (1975) and γ_0 is from Speziale et al. (2001). [2]Values are from Li and Zhang (2005). α_0 is from Fiquet et al. (1998) and γ_0 is from Tange et al. (2012). [3]Values for K_{0T} and K_{0T}' are from Brown (1999) and were obtained by fitting pressure-volume data, from which K_{0S} and K_{0S}' were calculated. G_0 and G_0' were obtained by fitting Kinoshita et al.'s (1979) ultrasonic data. Uncertainties in K_0' and G_0' are propagated. α_0 and γ_0 are from Boehler and Kennedy (1980). [4]Values are from Jiang et al. (2009). α_0 is from Ito et al. (1974) and γ_0 is from Watanabe (1982). [5]Values for ρ_0, K_0, and K_0' were obtained from Hemley et al. (1987). G_0 and G_0' were obtained by fitting the data from Kuriakose et al. (2017). K_{0S} and K_{0S}' were calculated from K_{0T} and K_{0T}' obtained from the literature. α_0 and γ_0 are from Fei et al. (1993). [6]Values are from Marquardt et al. (2013). K_{0S} was calculated from K_{0T} given in the literature. α_0 is from Marquardt et al. (2013), and γ_0 is from Ross et al. (1986). [7]Values are from Sasaki et al. (2008). K_0' and G_0' were obtained by fitting the data. Their uncertainties are propagated from the literature. α_0 is from Packard and Swenson (1963), and γ_0 is from Anderson and Swenson (1975). [8]Values are from Zha et al. (1993). K_0' and G_0' were obtained by fitting the data. Their uncertainties are propagated from the literature. α_0 and γ_0 are also from Zha et al. (1993). [9]Values are from Zha et al. (2004). K_0' and G_0' were obtained by fitting the data. Their uncertainties are propagated from the literature. α_0 and γ_0 are also from Zha et al. (2004).

$$\%Dev. = \sum_{i=1}^{n} 100^{*} \frac{|calc_i - data_i|}{|data_i|} \tag{32}$$

$$RMSrD = \sqrt{\frac{\sum_{i=1}^{n} \frac{(calc_i - data_i)^2}{data_i}}{n-1}}. \tag{33}$$

The misfits are displayed in each plot and summarized in Figure 11. There are some cases for which a calculated modulus or sound velocity approaches infinity or negative infinity (e.g., the material-frame shear modulus for *Xe*), and such values are ignored. In these cases, the quoted misfit is therefore smaller than its actual value.

The values of the isentropic bulk modulus (K_{0S}) and its isothermal pressure derivative (K_{0S}') in Table 5 are experimentally determined from sound wave propagation in the statically (isothermally) compressed materials. The values were obtained directly from the literature, except where marked. In these cases, K_{0S} and K_{0S}' were calculated from the corresponding isothermal values K_{0T} and K_{0T}' through the following relations:

$$\frac{K_S}{K_T} = 1 + \alpha\gamma T \tag{34}$$

$$K_S^{'} \approx K_T^{'} - \alpha\gamma T\left(\frac{dlnC_V}{dlnV} + 2q - 1\right) \tag{35}$$

where α is the coefficient of thermal expansion, γ is the Gruneisen parameter, and T is the temperature, with values also obtained from the literature (T = 300 K). Equation (35) is derived thermodynamically from the relationship described in (34), in the quasi-harmonic, high-temperature limit; we assume here that the parameter $q = \frac{d\ \ln(\gamma)}{d\ \ln(V)}$ is equal to 1. The value for $\frac{d\ \ln C_V}{d\ \ln V}$ is obtained using the Debye-Grüneisen model, ignoring anharmonic terms. Equations (34) and (35) were also used for our calculations of static-compression isotherms.

3.2. Discussion

Significant work has previously been done to compare the results of either experimental measurements or first-principles (quantum mechanical) calculations against different functional forms for the pressure-

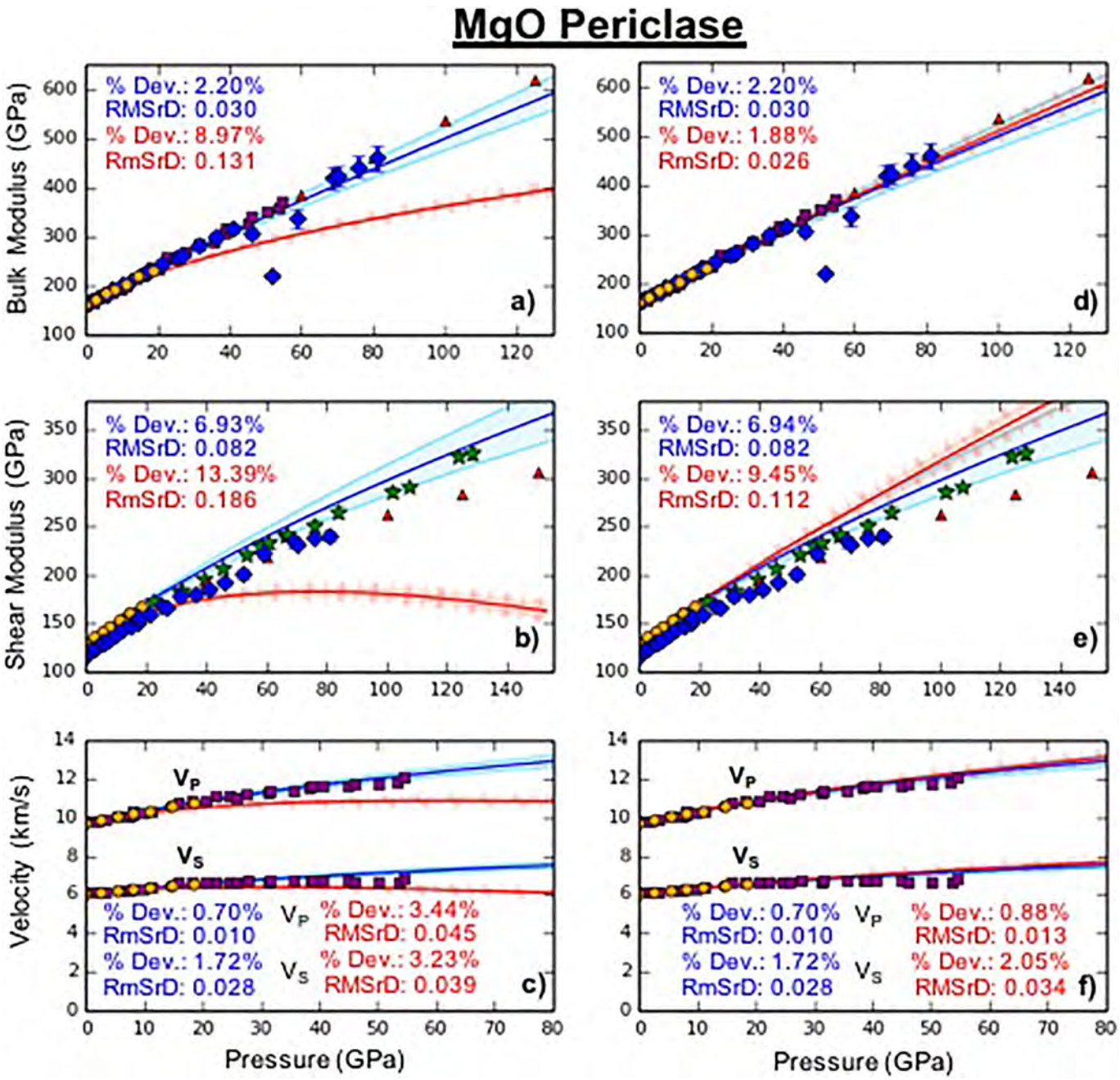

Figure 2. Measured and calculated elastic moduli and sound velocities for B1-structured MgO as a function of pressure at 300 K, with curves comparing calculated values derived from *spatial* (*Eulerian: blue*) and *material* (*Lagrangian: red*) formulations in (a) to (c) and from *self-consistent* (*blue*) versus *non-self-consistent* (*red*) Eulerian approaches in (d) to (f). The curves are derived from Brillouin scattering measurements of Sinogeikin and Bass (2000; *orange circles*), and extrapolated to higher pressures to compare with Brillouin measurements of Zha et al. (2000; *purple squares*), Murakami et al. (2009; *green stars*), and Marquardt et al. (2009; *blue diamonds*), as well as with first-principles calculations of Karki et al. (1997a; *red triangles*). Both longitudinal (V_P) and transverse (V_S) velocities are shown in (c) and (f). The study by Marquardt et al. (2009) examined $(Mg_{0.9}Fe_{0.1})O$, with the dip in bulk modulus around 45 GPa attributed to the high-spin to low-spin transition in octahedrally coordinated ferrous iron; there is also an offset in shear modulus values relative to other measurements. Percent deviation (% Dev) and root-mean-square deviation (RMSrD) of data relative to curves are listed in text of the same color as the relevant curve, and shaded envelopes represent uncertainties for the curves (uncertainties for the measurements are smaller than the symbols when not shown).

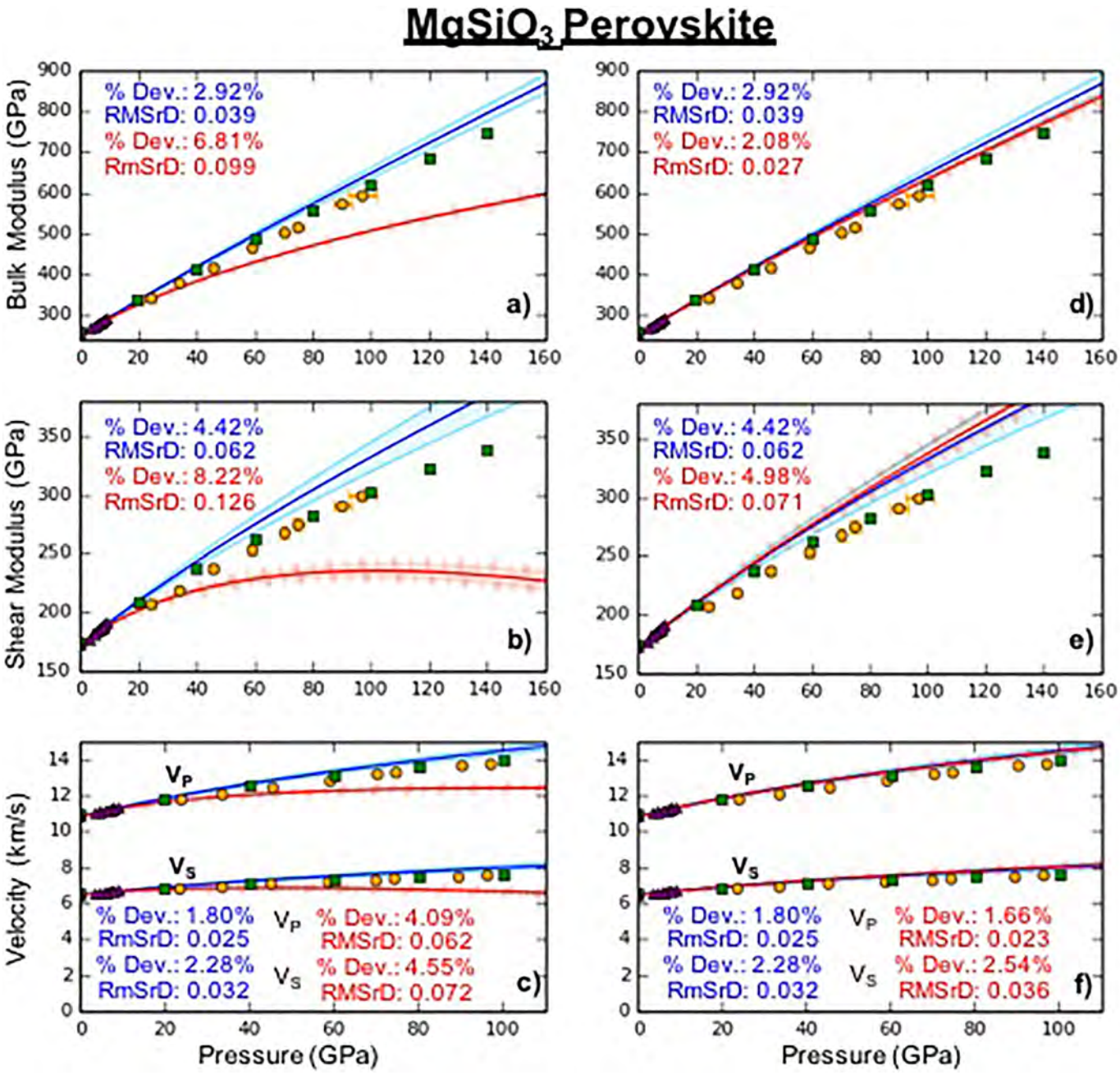

Figure 3. Measured and calculated elastic moduli and sound velocities for perovskite-structured $MgSiO_3$ as a function of pressure at 300 K, with curves comparing calculated values derived from *spatial* (*Eulerian: blue*) and *material* (*Lagrangian: red*) formulations in a to c, and from *self-consistent* (*blue*) versus *non-self-consistent* (*red*) Eulerian approaches in d to f. The curves are derived from ultrasonic interferometry measurements of Li and Zhang (2005; *purple triangles*) and extrapolated to higher pressures to compare with Brillouin measurements of Murakami et al. (2007; *orange circles*) and the first-principles calculations of Karki et al. (1997b; *green squares*). Both longitudinal (V_P) and transverse (V_S) velocities are shown in (c) and (f). Percent deviation (% Dev) and root-mean-square deviation (RMSrD) of data relative to curves are listed in text of the same color as the relevant curve, and shaded envelopes represent estimated uncertainties for the curves (uncertainties for the measurements are smaller than the symbols when not shown).

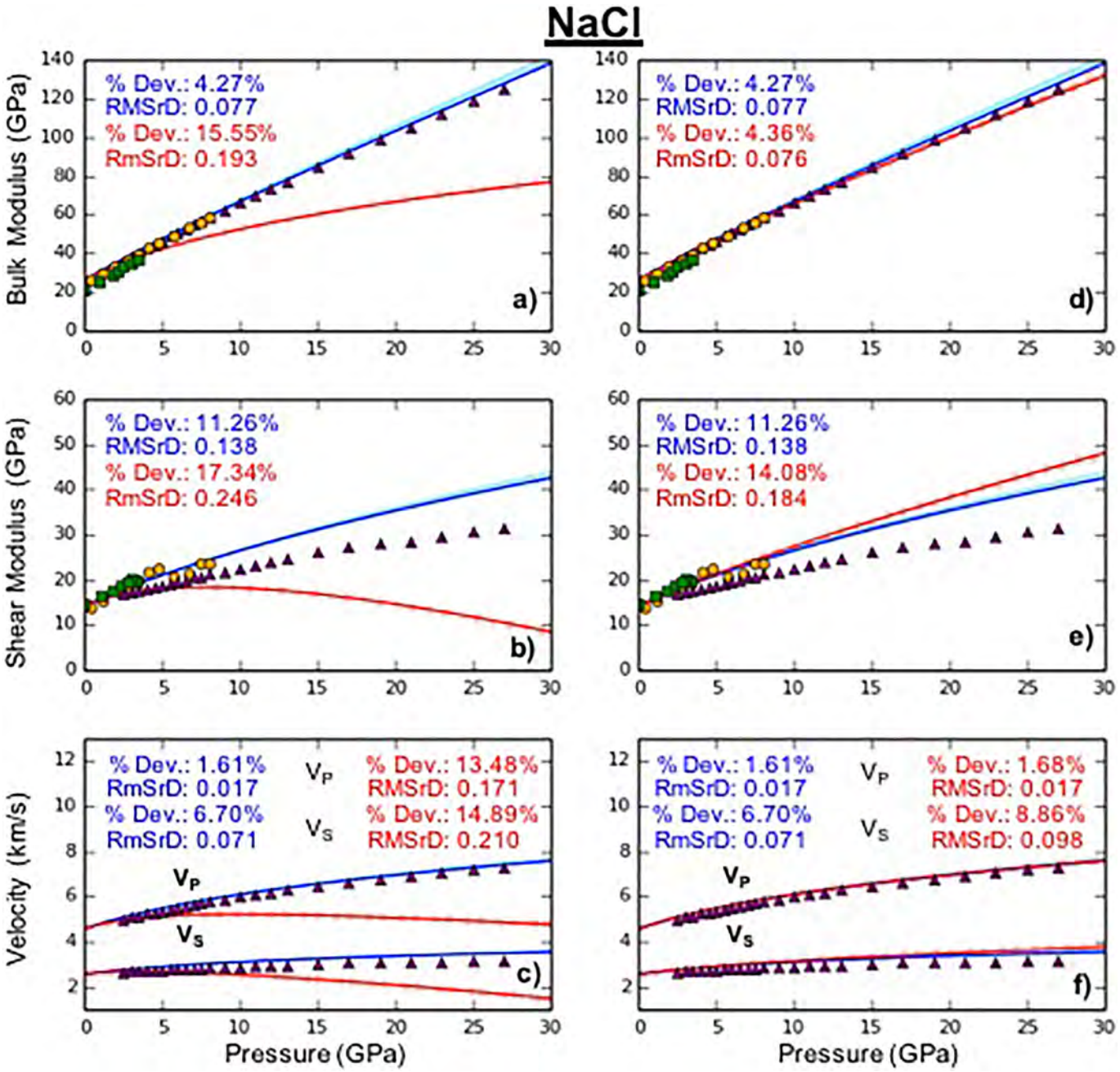

Figure 4. Measured and calculated elastic moduli and sound velocities for B1-structured NaCl as a function of pressure at 300 K, with curves comparing calculated values derived from *spatial* (*Eulerian: blue*) and *material* (*Lagrangian: red*) formulations in (a) to (c) and from *self-consistent* (*blue*) versus *non-self-consistent* (*red*) Eulerian approaches in (d) to (f). The curves are derived from a combination of the pressure-volume data compiled by Brown (1999) and the of ultrasonic interferometry measurements of Kinoshita et al. (1979; *orange circles*) and extrapolated to lower and higher pressures to compare with Brillouin measurements of Whitfield et al. (1976; *green squares*) and the ultrasonic measurements of Frankel et al. (1976; *purple triangles*). The shear modulus measurements from Kinoshita et al. (1979) and Whitfield et al. (1976) are averaged using the Voigt-Reuss-Hill scheme. Both longitudinal (V_P) and transverse (V_S) velocities are shown in (c) and (f). Percent deviation (% Dev) and root-mean-square deviation (RMSrD) of data relative to curves are listed in text of the same color as the relevant curve, and shaded envelopes represent estimated uncertainties for the curves (uncertainties for the measurements are smaller than the symbols when not shown).

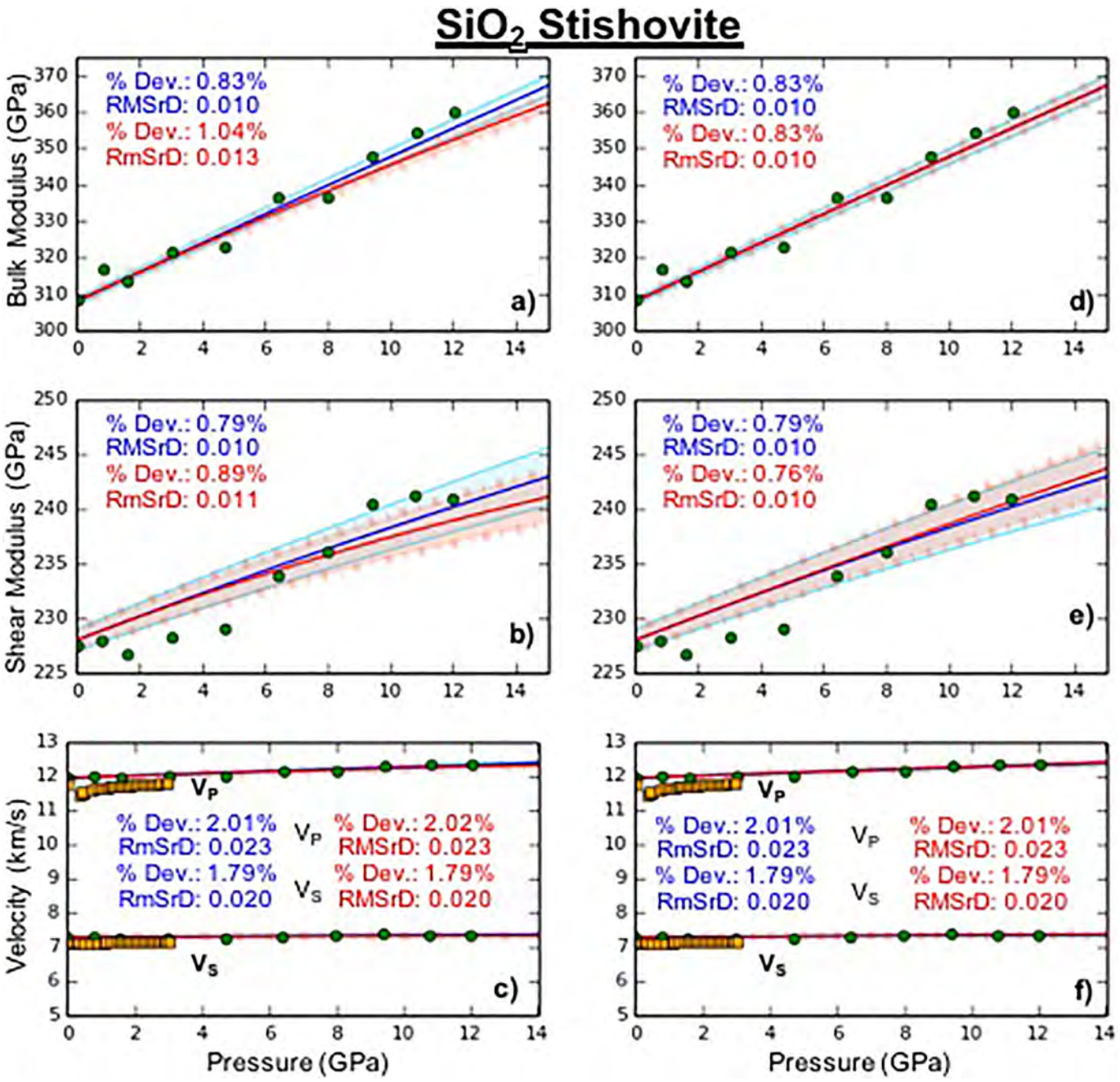

Figure 5. Measured and calculated elastic moduli and sound velocities for rutile-structured SiO_2 as a function of pressure at 300 K, with curves comparing calculated values derived from *spatial* (*Eulerian: blue*) and *material* (*Lagrangian: red*) formulations in (a) to (c) and from *self-consistent* (*blue*) versus *non-self-consistent* (*red*) Eulerian formulations in (d) to (f). The curves are derived from the Brillouin scattering measurements of Jiang et al. (2009) *(green circles)* and extrapolated to lower and higher pressures to compare with the ultrasonic interferometry measurements of Li et al. (1996; *orange squares*). Both longitudinal (V_P) and transverse (V_S) velocities are shown in (c) and (f). Percent deviation (% Dev) and root-mean-square deviation (RMSrD) of data relative to curves are listed in text of the same color as the relevant curve, and shaded envelopes represent estimated error envelopes for the curves (uncertainties for the measurements are smaller than the symbols when not shown).

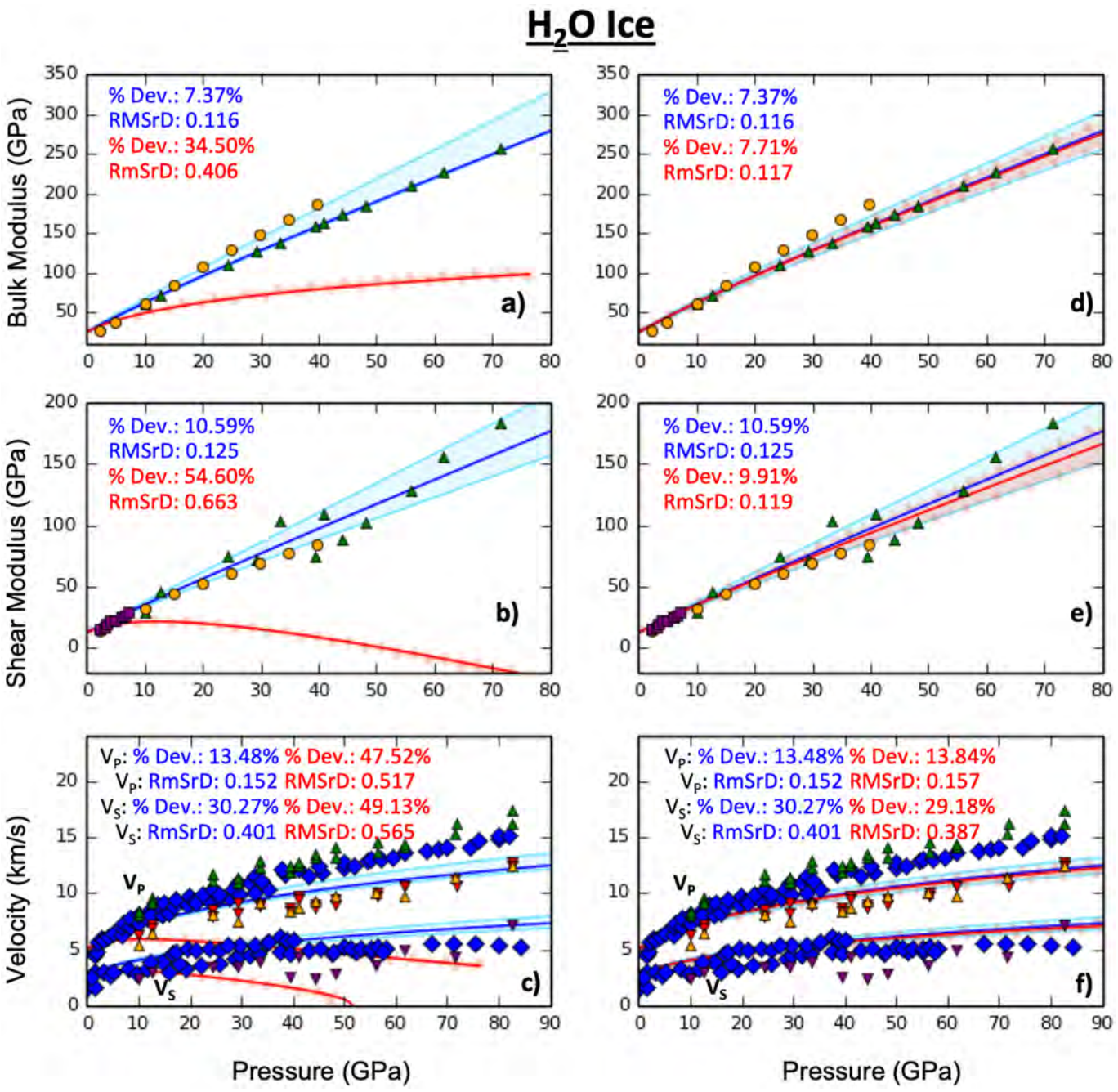

Figure 6. Measured and calculated elastic moduli and sound velocities for cubic ice-VII-structured H_2O as a function of pressure at 300 K, with curves comparing calculated values derived from *spatial* (*Eulerian: blue*) and *material* (*Lagrangian: red*) formulations in (a) to (c) and from *self-consistent* (*blue*) versus *non-self-consistent* (*red*) Eulerian approaches in (d) to (f) . The curves are derived from the pressure-volume measurements of Hemley et al. (1987) and the Brillouin scattering measurements of Kuriakose et al. (2017; *green triangles*) and extrapolated to lower and higher pressures to compare with the Brillouin measurements of Zha et al. (1998; *orange circles*), Ahart et al. (2011; *blue diamonds*), and Shimizu et al. (1995; *purple squares*). The shear modulus measurements from Kuriakose et al. (2017), Zha et al. (1998), and Shimizu et al. (1995) are averaged using the Voigt-Reuss-Hill scheme. Both longitudinal (V_P) and transverse (V_S) velocities are shown in (c) and (f). The maximum and minimum V_P (*green and red*) and V_S *(orange and purple)* velocities from Kuriakose et al. (2017) are plotted at each pressure (*upward- and downward-facing triangles, respectively*), accounting for the rotational variance in single-crystal velocities. Percent deviation (% Dev) and root-mean-square deviation (RMSrD) of data relative to curves are listed in text of the same color as the relevant curve, and shaded envelopes represent estimated uncertainties for the curves (uncertainties for the measurements are smaller than the symbols when not shown).

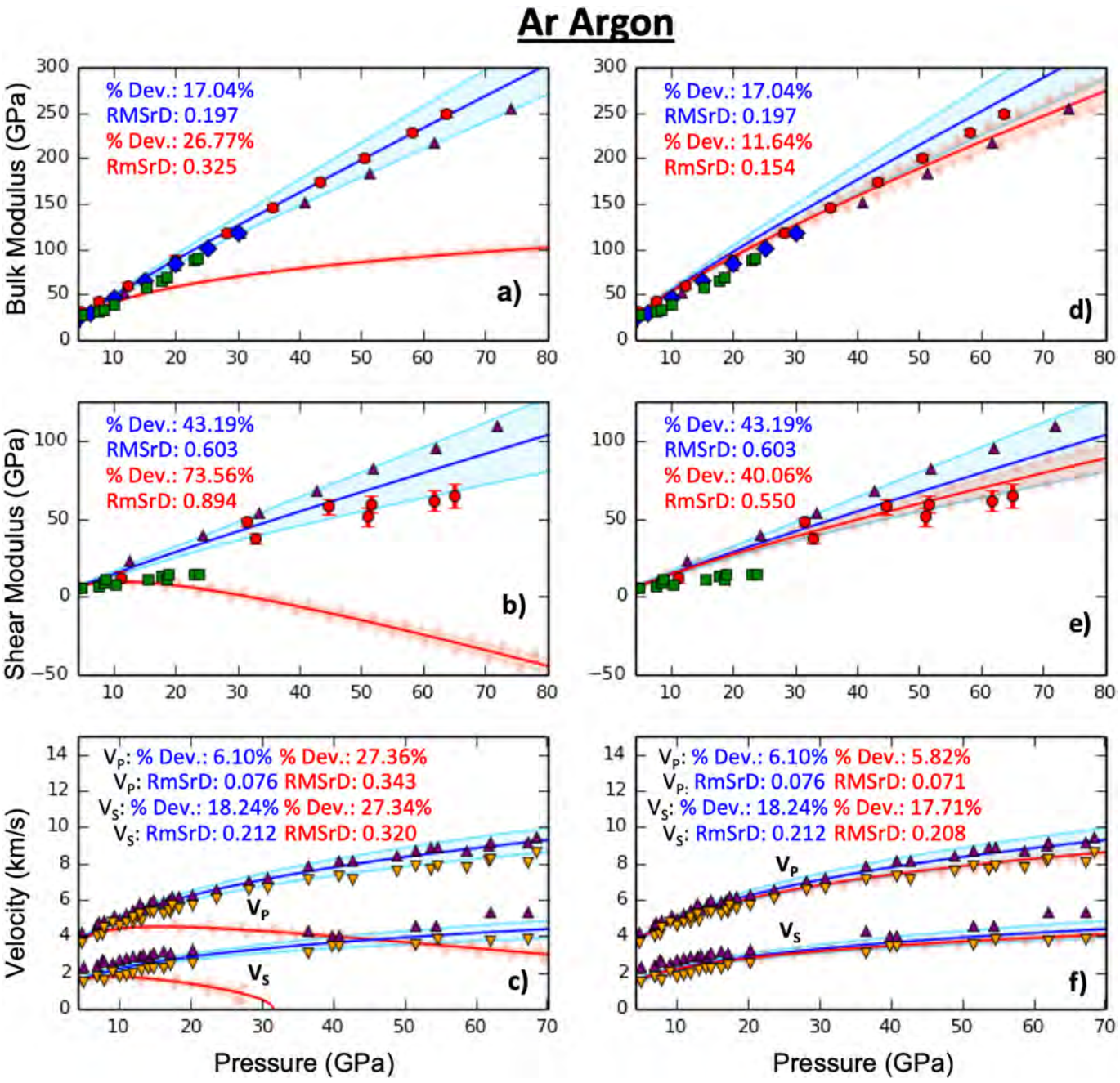

Figure 7. Measured and calculated elastic moduli and sound velocities for fcc-structured Ar as a function of pressure at 300 K, starting from initial pressure $P_0 = 4.3$ GPa, with curves comparing calculated values derived from *spatial* (*Eulerian: blue*) and *material* (*Lagrangian: red*) formulations in (a) to (c) and from *self-consistent* (*blue*) versus *non-self-consistent* (*red*) Eulerian formulations in (d) to (f). The curves are derived from Brillouin scattering measurements of Marquardt et al. (2013; *red circles*) and extrapolated to higher and lower pressures to compare with Brillouin measurements of Shimizu et al. (2001; *purple triangles*), Chen et al. (2010; *green squares*), and Grimsditch et al. (1986; *blue diamonds*). The shear modulus measurements from Shimizu et al. (2001) were averaged using the Voigt-Reuss-Hill scheme. Both longitudinal (V_P) and transverse (V_S) velocities are shown in (c) and (f). The maximum and minimum velocities from Shimizu et al. (2001) are plotted at each pressure (*purple and orange upward- and downward-facing triangles, respectively*), accounting for the rotational variance in single-crystal velocities. Percent deviation (% Dev) and root-mean-square deviation (RMSrD) of data relative to curves are listed in text of the same color as the relevant curve, and shaded envelopes represent estimated uncertainties for the curves (uncertainties for the measurements are smaller than the symbols when not shown).

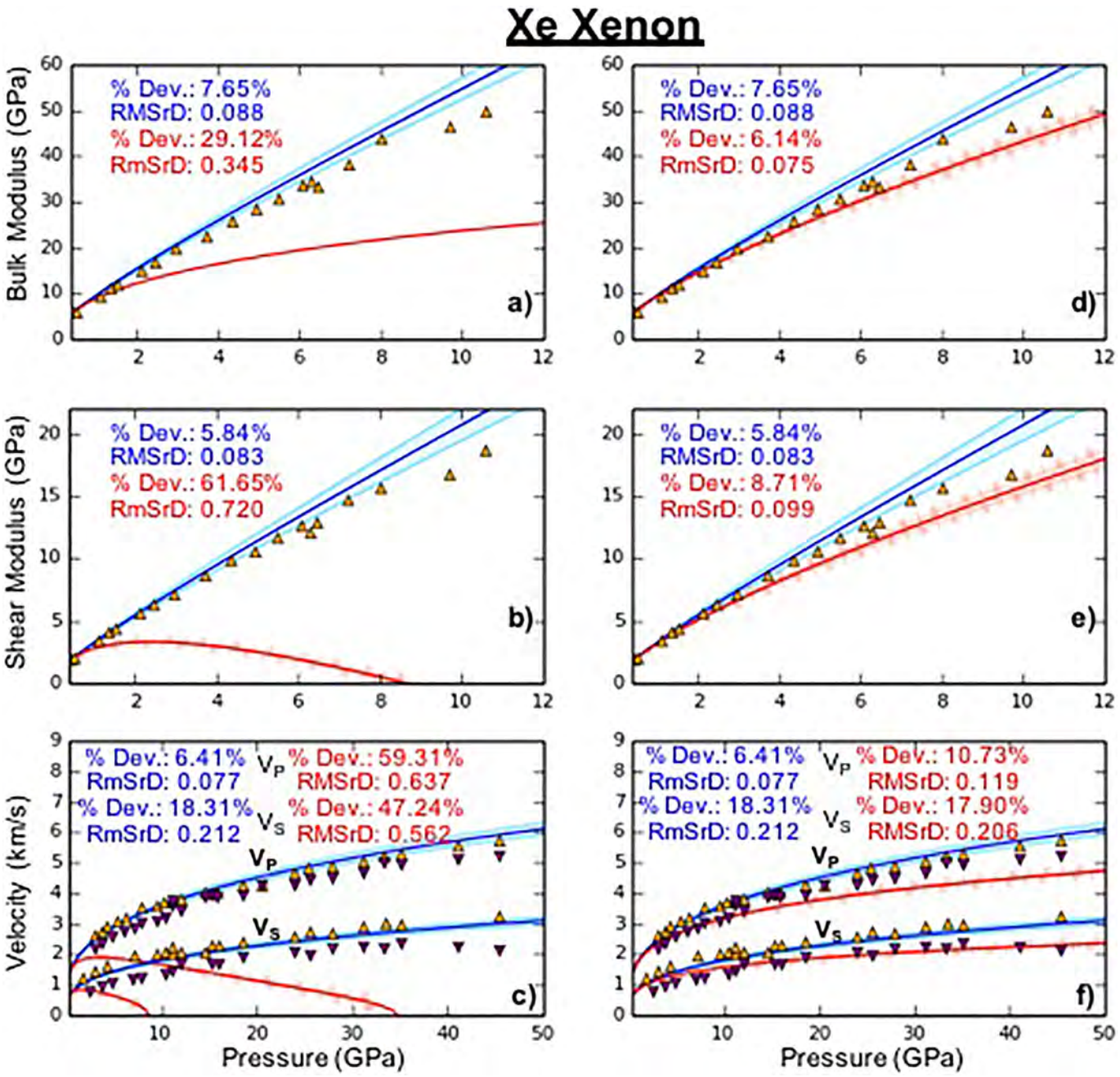

Figure 8. Measured and calculated elastic moduli and sound velocities for fcc Xe as a function of pressure at 300 K, starting from initial pressure $P_0 = 0.45$ GPa, with curves comparing calculated values derived from *spatial* (*Eulerian: blue*) and *material* (*Lagrangian: red*) formulations in (a) to (c) and from *self-consistent* (*blue*) versus *non-self-consistent* (*red*) Eulerian formulations in (d) to (f). The curves are derived from Brillouin scattering measurements of Sasaki et al. (2008; *orange triangles*) and extrapolated to higher and lower pressures. The shear modulus measurements were averaged using the Voigt-Reuss-Hill scheme. Both longitudinal (V_P) and transverse (V_S) velocities are shown in (c) and (f). The maximum and minimum velocities are plotted at each pressure (*purple and orange upward- and downward-facing triangles, respectively*), accounting for the rotational variance in single-crystal velocities. Percent deviation (% Dev) and root-mean-square deviation (RMSrD) of data relative to curves are listed in text of the same color as the relevant curve, and shaded envelopes represent estimated uncertainties for the curves (uncertainties for the measurements are smaller than the symbols when not shown).

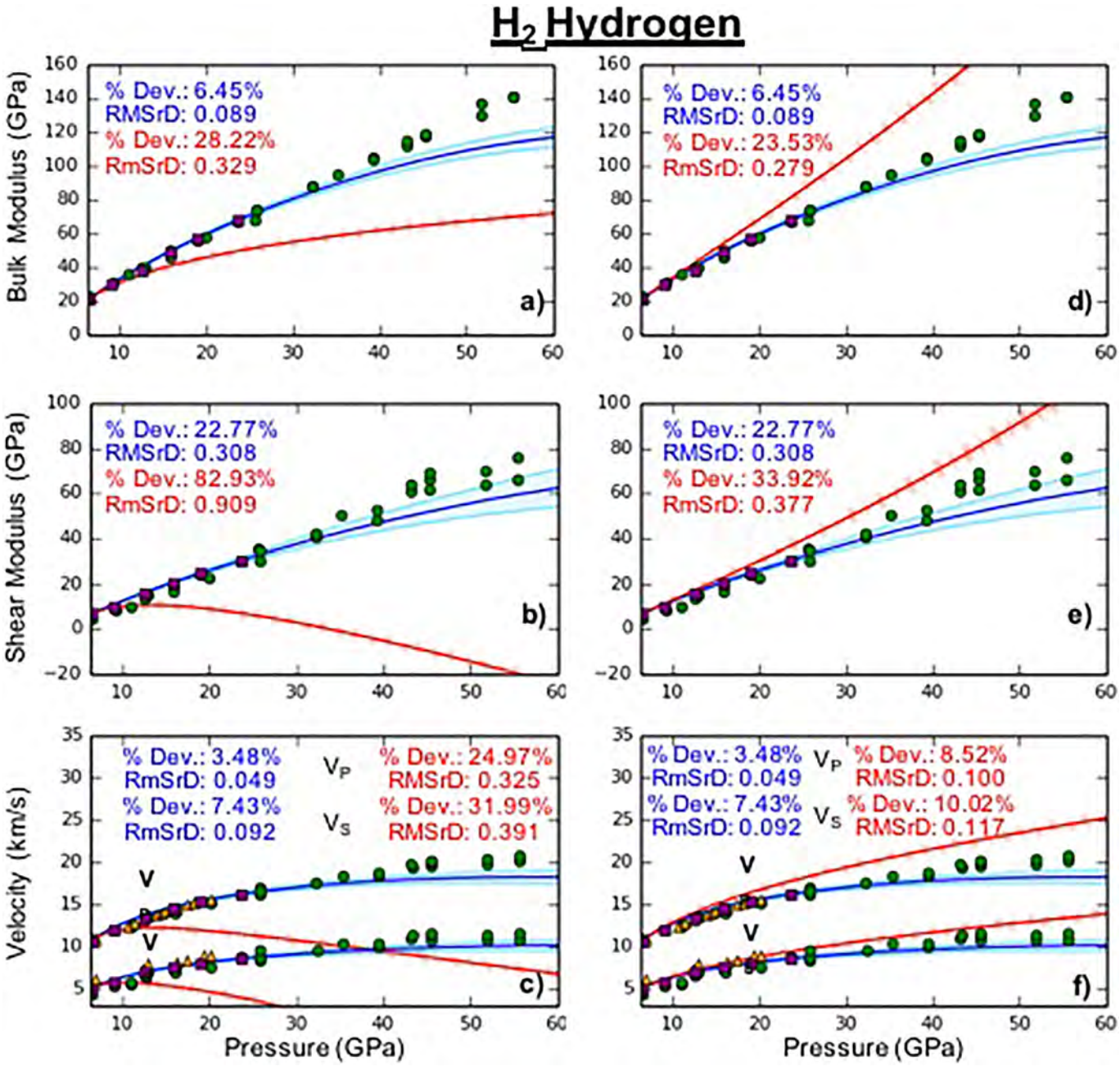

Figure 9. Measured and calculated elastic moduli and sound velocities for hcp-H_2 as a function of pressure at 300 K, starting from initial pressure $P_0 = 6.4$ GPa, with curves comparing calculated values derived from *spatial* (*Eulerian: blue*) and *material* (*Lagrangian: red*) formulations in (a) to (c) and from *self-consistent* (*blue*) versus *non-self-consistent* (*red*) Eulerian formulations in (d) to (f). The curves are derived from Brillouin scattering measurements of Zha et al. (1993; *purple squares*) and extrapolated to higher and lower pressures to compare with Brillouin measurements of Shimizu et al. (1981; *orange triangles*) and Goncharov et al. (2017; *green circles*). The shear modulus measurements from Goncharov et al. (2017) were averaged by the Voigt-Reuss-Hill scheme. Both longitudinal (V_P) and transverse (V_S) velocities are shown in (c) and (f). Percent deviation (% Dev) and root-mean-square deviation (RMSrD) of data relative to curves are listed in text of the same color as the relevant curve, and shaded envelopes represent estimated uncertainties for the curves (uncertainties for the measurements are smaller than the symbols when not shown).

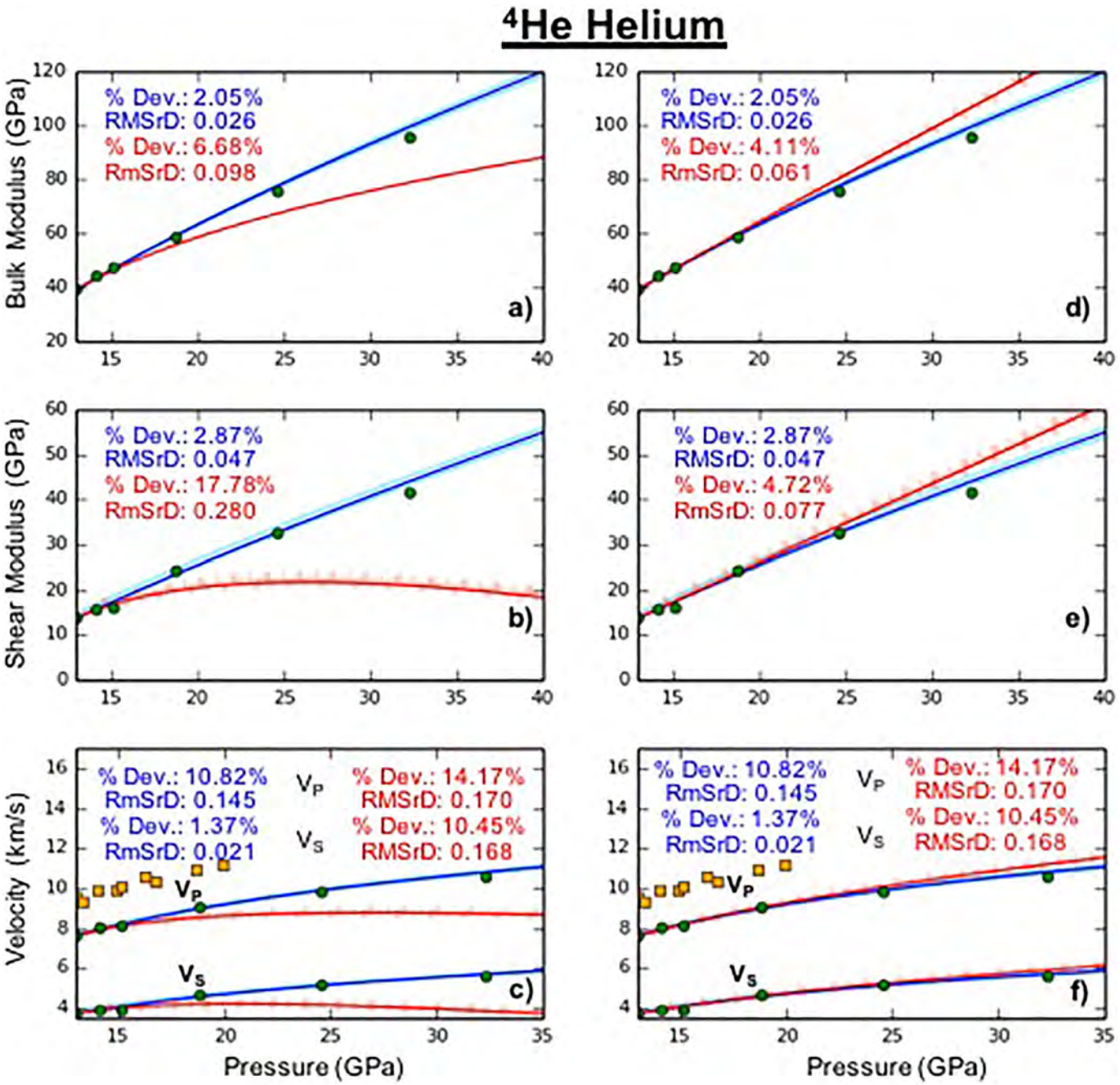

Figure 10. Measured and calculated elastic moduli and sound velocities for hcp-^{4}He as a function of pressure at 300 K, starting from initial pressure $P_0 = 13$ GPa, with curves comparing calculated values derived from *spatial* (*Eulerian: blue*) and *material* (*Lagrangian: red*) formulations in (a) to (c) and from *self-consistent* (*blue*) versus *non-self-consistent* (*red*) Eulerian formulations in (d) to (f). The curves are derived from Brillouin scattering measurements of Zha et al. (2004; *green circles*). They are extrapolated to compare with Brillouin longitudinal (V_P) velocity measurements of Polian and Grimsditch (1986) (*orasnge squares*). Both longitudinal (V_P) and transverse (V_S) velocities are shown in (c) and (f). Percent deviation (% Dev) and root-mean-square deviation (RMSrD) of data relative to curves are listed in text of the same color as the relevant curve, and shaded envelopes represent estimated uncertainties for the curves (uncertainties for the measurements are smaller than the symbols when not shown).

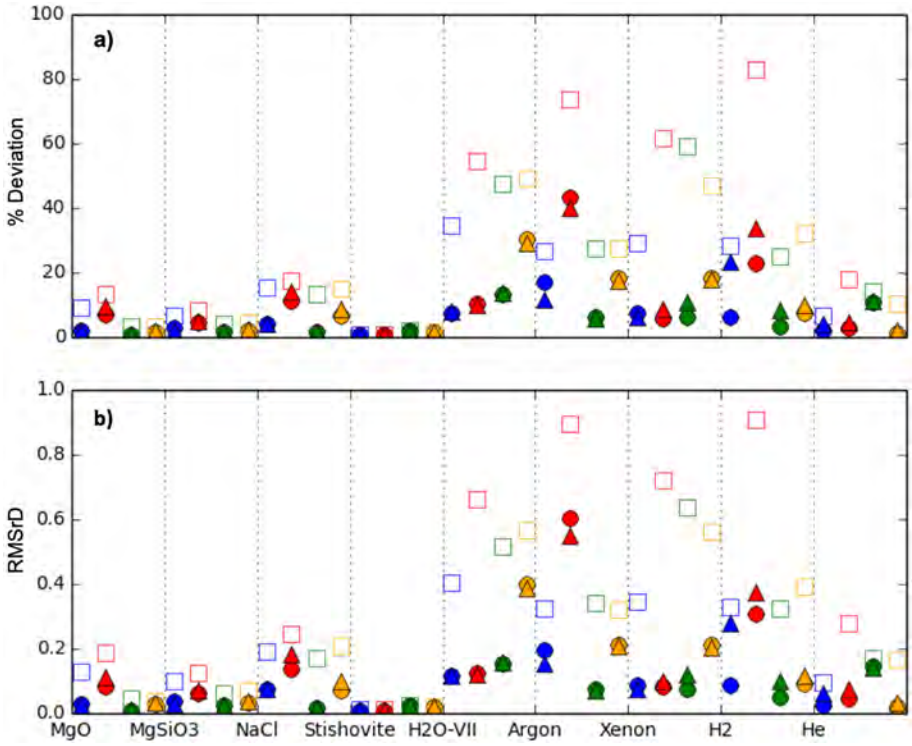

Figure 11. Misfit between calculated and measured *bulk moduli (blue)*, *shear moduli (red)*, *longitudinal velocity (green)*, and *transverse velocity (orange)* for each material analyzed in the present study. Misfits are shown for *self-consistent Eulerian (solid circles)*, *self-consistent Lagrangian (open squares)*, and *non-self-consistent Eulerian (solid triangles) calculations*. Values in (a) are measured by percent deviation in absolute value, while those in (b) are the root-mean-square deviation.

volume equations of state of condensed matter (e.g., Birch, 1978; Davies, 1973a; Jeanloz, 1989; Latimer et al., 2018). The general result is that the Eulerian finite-strain formulation is consistent with combined infinitesimal- and finite-strain measurements, whereas other popular forms are not (e.g., Murnaghan, Slater, and Lagrangian finite-strain). Rather than further refining these comparisons, the present work shifts attention to determining how well the various equation-of-state formulations reproduce the measured shear properties of condensed matter under finite compression.

The results in Figures 2–10 indicate that the spatial (Eulerian) reference frame unambiguously fits better than the material (Lagrangian) reference frame for most materials. With the exception of stishovite, every material displays substantially larger misfits using material formulas, with average percent deviations ranging from about 5% larger for the stiffer and more incompressible materials to 50% for the softer, more compressible materials. The comparison of spatial and material formulations to data for the bulk and shear moduli of bridgmanite closely match the study by Stixrude and Lithgow-Bertelloni (2010). In the case of stishovite (Figure 5), the reference frames show comparable fits to the data, differing within the error of the calculations. Of the materials examined here, stishovite also has the highest bulk and shear moduli, and the divergence between different equations of state is small at Earth-mantle pressures. It is therefore notable that the spatial formulations fit better than the material formulations, because in principle they should be capable of providing equally good fits if enough terms are included in the energy expansion.

As has been noted by others (e.g., Jackson, 1998), the third-order coefficient for the *P-V* equation of state is roughly one order of magnitude smaller for the spatial as compared to the materials formulation, that is, K_{0S}'~ 4 rather than K_{0S}'~ 0 (Table 5), and the success of the spatial finite-strain approach has often been ascribed to this empirical fact. However, the third-order coefficients for the finite strain expansions of bulk and shear moduli are comparable (albeit slightly smaller) for spatial versus material expressions, vanishing for $K_{0S}' = 5/3$ versus $K_{0S}' = 1/3$ and $K_{0S}'G_0' = 5G_0/3$ versus $K_{0S}'G_0' = G_0/3$, respectively. Also, the values of $K_{0S}'G_0'$ and of G_0' vary by more than one order of magnitude for the materials considered here. Therefore,

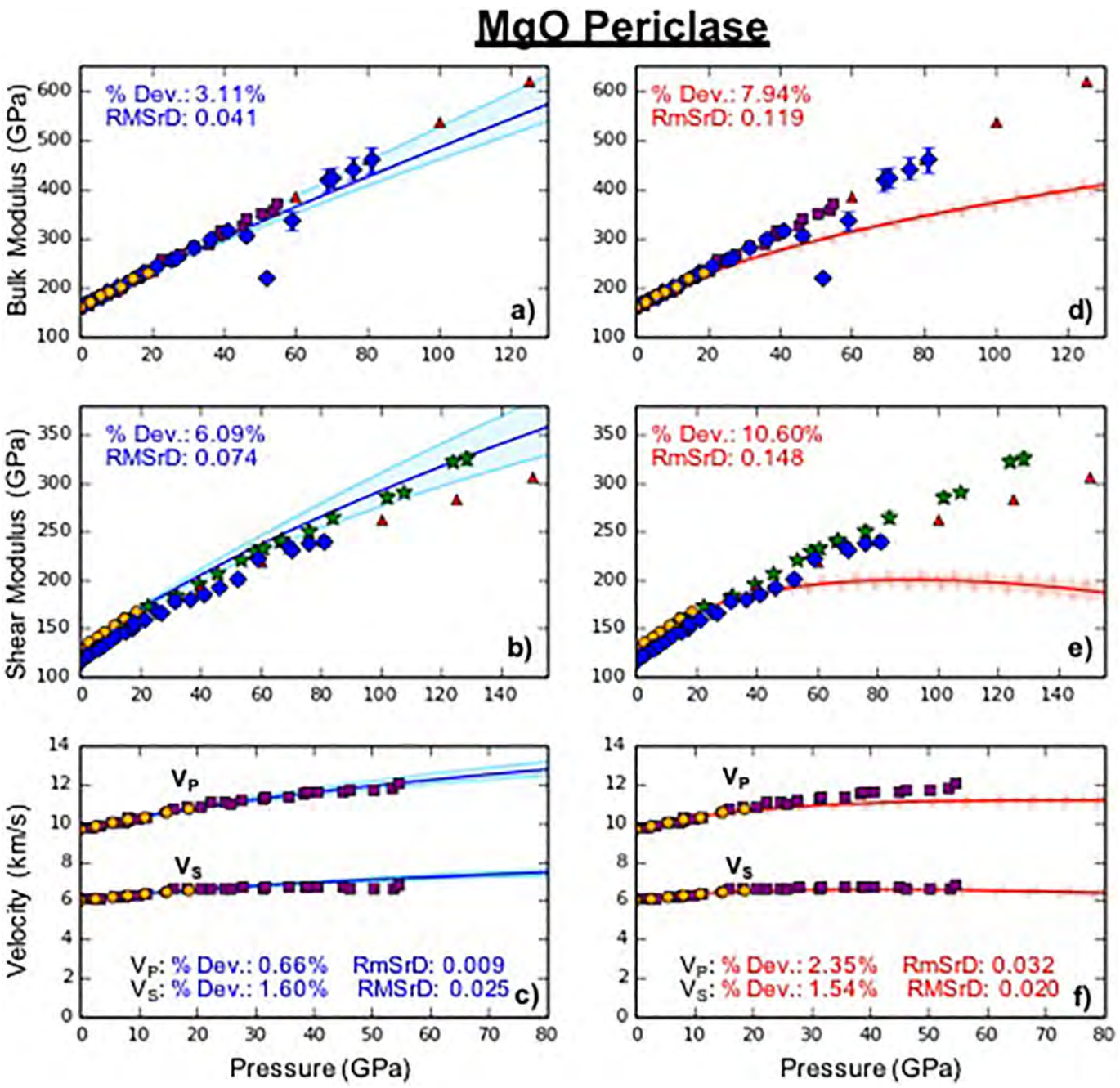

Figure 12. Measured and calculated elastic moduli and sound velocities for B1-structured MgO as a function of pressure at 300 K, with curves comparing calculated values derived from *spatial/Eulerian* (*blue*) and *material/Lagrangian* (*red*) formulations. The calculations are obtained and extrapolated by fitting the Brillouin measurements of Sinogeikin and Bass (2000; *orange circles*) with Eulerian equations in (a–c) and with Lagrangian equations in (d–f). The curves are compared at higher pressures with the Brillouin measurements of Zha et al. (2000; *purple squares*), Murakami et al. (2009; *green stars*), and Marquardt et al. (2009; *blue diamonds*), as well as with first-principles calculations of Karki et al. (1997a; *red triangles*). Both longitudinal (V_P) and transverse (V_S) velocities are shown in (c) and (f). The study by Marquardt et al. (2009) examined $(Mg_{0.9}Fe_{0.1})O$, which exhibits a dip in bulk modulus measurements around 45 GPa attributed to the iron spin transition, and an offset of shear modulus values relative to the other studies. Percent deviation (% Dev) and root-mean-square deviation (RMSrD) of data relative to curves are listed in text of the same color as the relevant curve, and shaded envelopes represent estimated uncertainties for the curves (uncertainties for the measurements are smaller than the symbols when not shown).

the arguments that the Eulerian (spatial) formulation is preferred over the Lagrangian (material) formulation simply due to the coincidence of one material property having appropriate values (K_{0S}'~ 4) may be less compelling than previously thought.

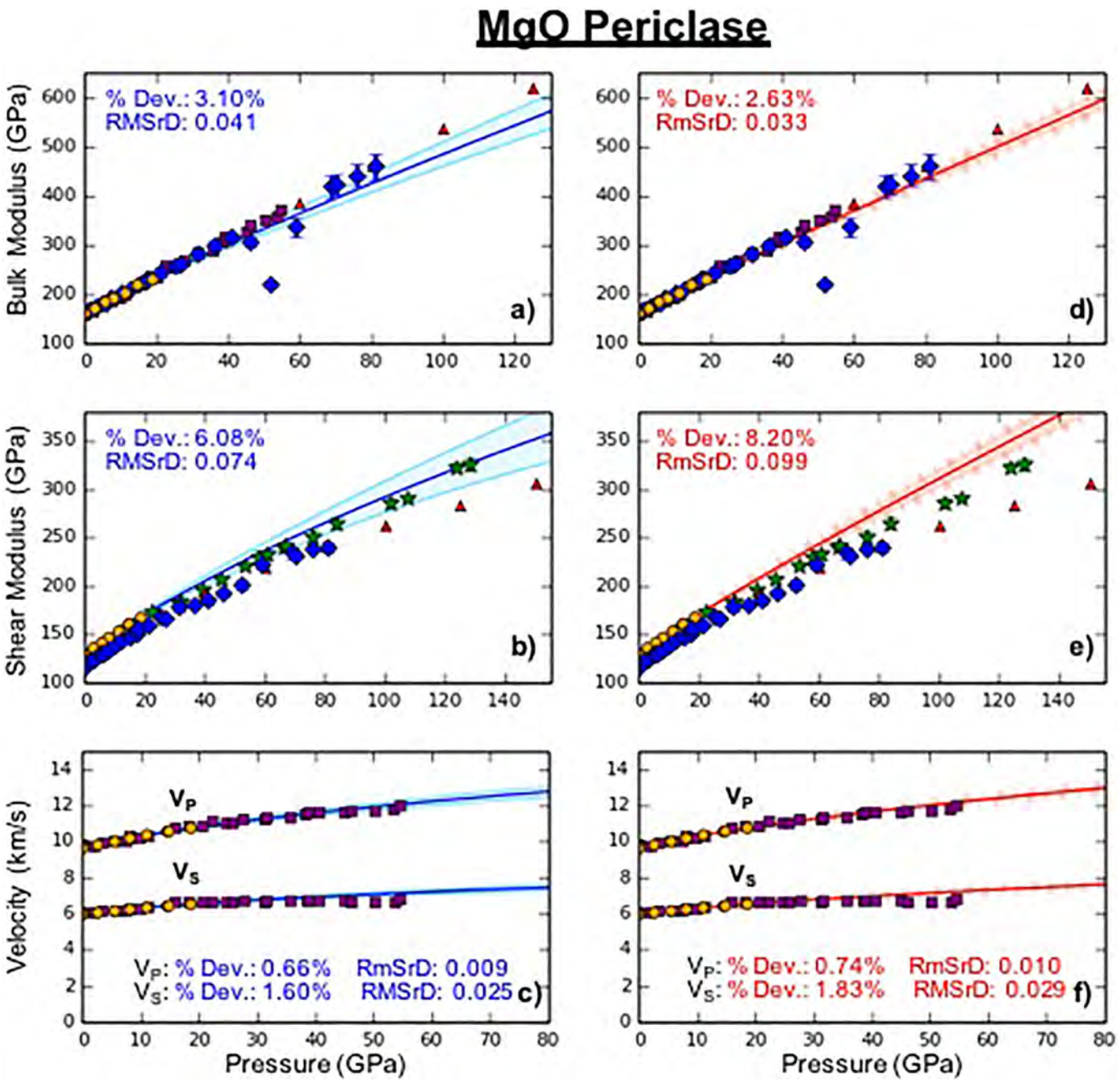

Figure 13. Measured and calculated elastic moduli and sound velocities for B1-structured MgO as a function of pressure at 300 K, with curves comparing calculated values derived from *self-consistent* (*blue*) and *non-self-consistent* (*red*) approaches. The calculations were obtained and extrapolated by fitting the Brillouin measurements of Sinogeikin and Bass (2000; *orange circles*) with self-consistent equations in (a–c) and with non-self-consistent equations in (d–f). The curves are compared at higher pressures with the Brillouin measurements of Zha et al. (2000; *purple squares*), Murakami et al. (2009; *green stars*), and Marquardt et al. (2009; *blue diamonds*), as well as with first-principles calculations of Karki et al. (1997a; *red triangles*). Both longitudinal (V_P) and transverse (V_S) velocities are shown in (c) and (f). The study by Marquardt et al. (2009) examined $(Mg_{0.9}Fe_{0.1})O$, which exhibits a dip in bulk modulus measurements around 45 GPa attributed to the iron spin transition and an offset of shear modulus values relative to other studies. Percent deviation (% Dev) and root-mean-square deviation (RMSrD) of data relative to curves are listed in text of the same color as the relevant curve, and shaded envelopes represent estimated uncertainties for the curves (uncertainties for the measurements are smaller than the symbols when not shown).

In comparing self-consistent and non-self-consistent approaches, the distinction is less obvious than between spatial and material frames. In many cases, the moduli and sound velocities show comparable misfits, differing by only a few percent. In the case of hcp H_2, however, the difference is substantial (over 10% in

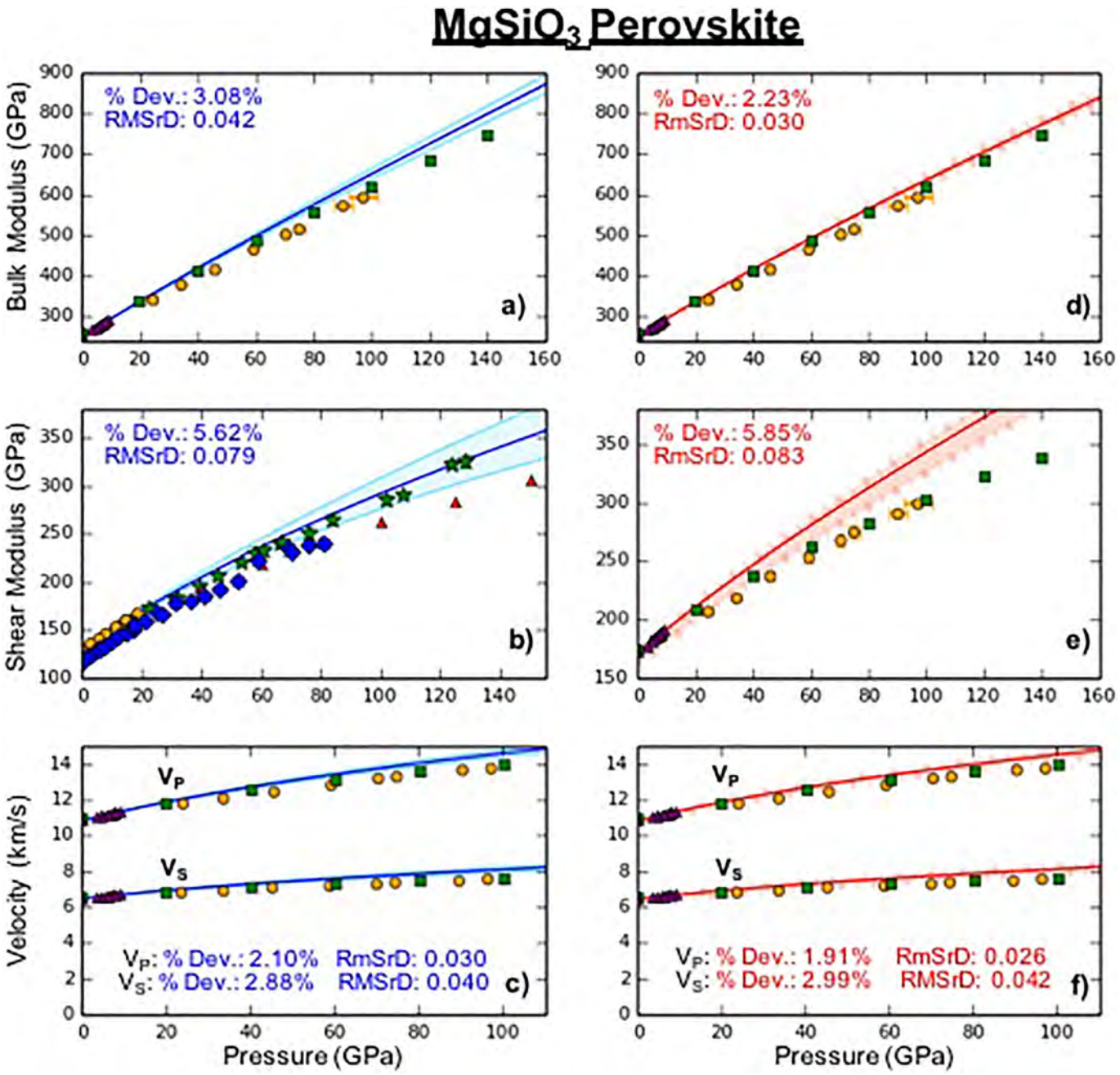

Figure 14. Measured and calculated elastic moduli and sound velocities for perovskite-structured $MgSiO_3$ as a function of pressure at 300 K, with curves comparing calculated values derived from *self-consistent* (*blue*) and *non-self-consistent* (*red*) approaches. The calculations were obtained and extrapolated by fitting the ultrasonic interferometry measurements of Li and Zhang (2005) (*purple triangles*) with self-consistent equations in (a–c) and with non-self-consistent equations in (d–f). The curves are compared with the Brillouin measurements of Murakami et al. (2007; *orange circles*) and the first-principles calculations of Karki et al. (1997b; *green squares*). Both longitudinal (V_P) and transverse (V_S) velocities are shown in (c) and (f). Percent deviation (% Dev) and root-mean-square deviation (RMSrD) of data relative to curves are listed in text of the same color as the relevant curve, and shaded envelopes represent estimated uncertainties for the curves (uncertainties for the measurements are smaller than the symbols when not shown).

the moduli) and favors the self-consistent approach. To a lesser extent, fcc Ar favors the non-self-consistent approach by about 5% in the moduli. It is difficult to specify a preference based only on these comparisons, but the results indicate empirically that the self-consistent moduli perform at least the non-self-consistent moduli. In addition, the self-consistent approach offers a unique definition of the higher-order elastic moduli, so in this regard it is preferable over the alternatives.

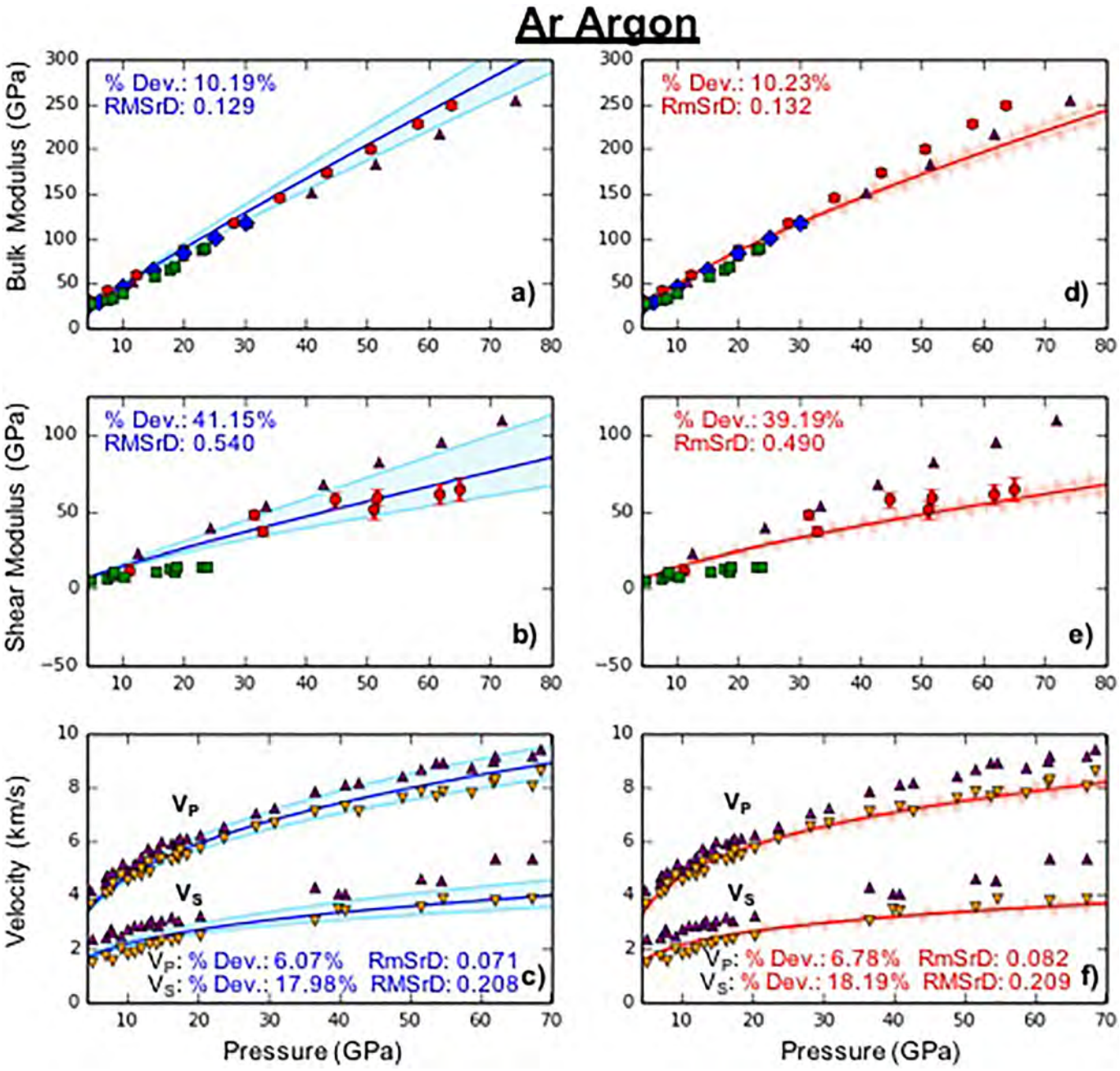

Figure 15. Measured and calculated elastic moduli and sound velocities for fcc-Ar as a function of pressure at 300 K, starting from initial pressure $P_0 = 4.3$ GPa, with curves comparing calculated values derived from *self-consistent* (*blue*) and *non-self-consistent* (*red*) approaches. The calculations were obtained and extrapolated by fitting the Brillouin scattering measurements of Marquardt et al. (2013; *red circles*) with self-consistent equations in a-c, and with non-self-consistent equations in (d–f). The curves are compared with Brillouin measurements of Shimizu et al. (2001; *purple triangles*), Chen et al. (2010; *green squares*), and Grimsditch et al. (1986; *blue diamonds*). The shear modulus measurements from Shimizu et al. (2001) were averaged using the Voigt-Reuss-Hill scheme. Both longitudinal longitudinal (V_P) and transverse (V_S) velocities are shown in (c) and (f). The maximum and minimum velocities from Shimizu et al. (2001) are plotted at each pressure (*purple and orange upward- and downward-facing triangles, respectively*), accounting for the rotational variance in single-crystal velocities. Percent deviation (% Dev) and root-mean-square deviation (RMSrD) of data relative to curves are listed in text of the same color as the relevant curve, and shaded envelopes represent estimated uncertainties for the curves (uncertainties for the measurements are smaller than the symbols when not shown).

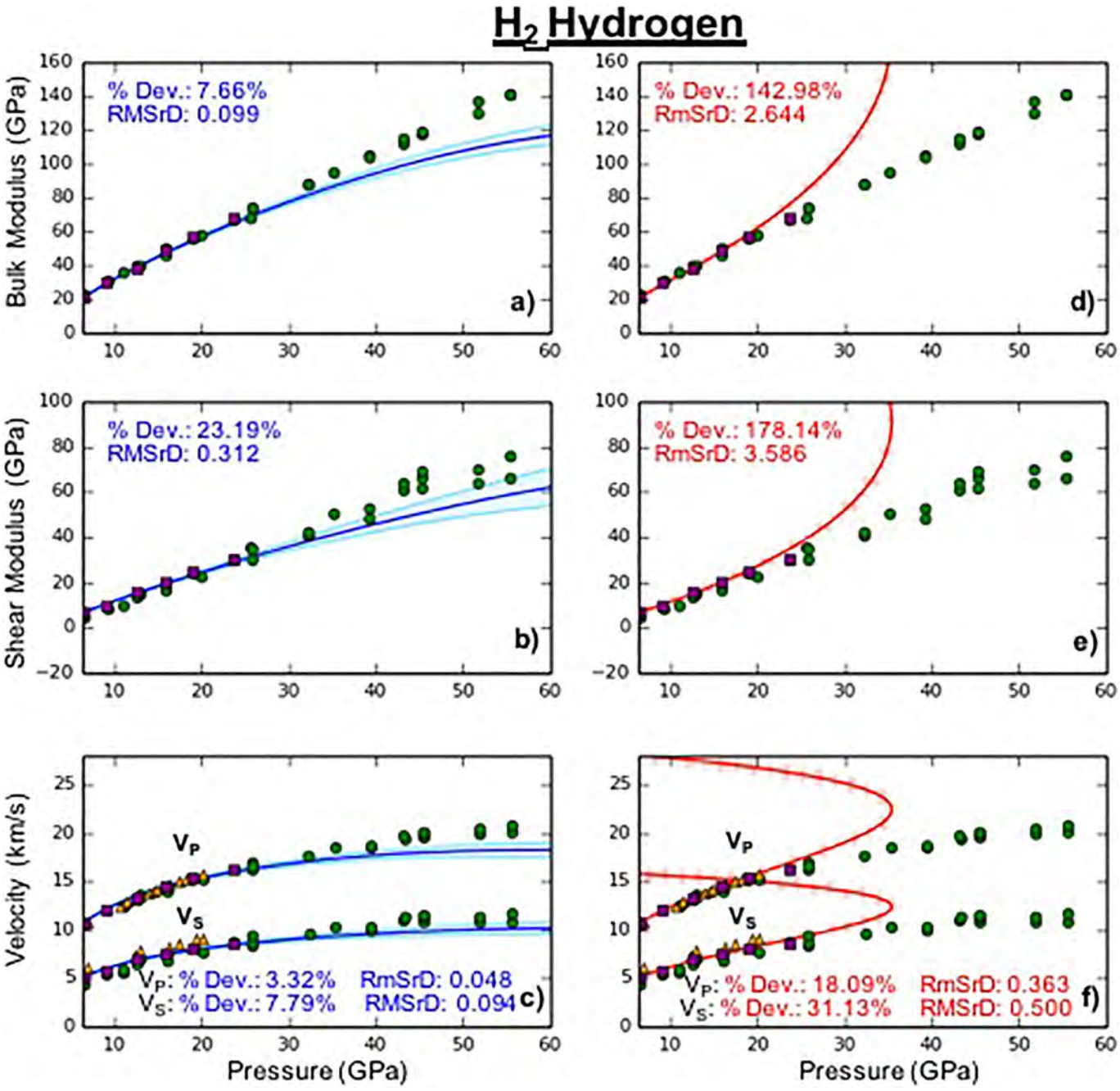

Figure 16. Measured and calculated elastic moduli and sound velocities for hcp-H_2 as a function of pressure at 300 K, starting from initial pressure $P_0 = 6.4$ GPa, with curves comparing calculated values derived from *self-consistent* (*blue*) and *non-self-consistent* (*red*) approaches. The calculations were obtained and extrapolated by fitting the Brillouin scattering measurements of Zha et al. (1993) (*purple squares*) with self-consistent equations in a-c, and with non-self-consistent equations in d-f. The curves are compared with Brillouin measurements of Shimizu et al. (1981; *orange triangles*) and Goncharov et al. (2017; *green circles*). The shear modulus measurements from Goncharov et al. (2017) were averaged using the Voigt-Reuss-Hill scheme. Both longitudinal (V_P) and transverse (V_S) velocities are shown in (c) and (f). Percent deviation (% Dev) and root-mean-square deviation (RMSrD) of data relative to curves are listed in text of the same color as the relevant curve, and shaded envelopes represent estimated uncertainties for the curves (uncertainties for the measurements are smaller than the symbols when not shown).

Table 6
Self-Consistent and Non-self-consistent Material Constants[a]

	K_{0S} (GPa)$^{+}$	K_{0S} (GPa)*	K_{0S}'$^{+}$	K_{0S}'*	G_0 (GPa) $^{+}$	G_0 (GPa) *	G_0'$^{+}$	G_0'*
MgO[1]	163.20 (10)	163.10 (10)	3.83 (15)	3.72 (15)	130.20 (10)	130.5 (10)	2.21 (10)	2.17 (10)
$MgSiO_3$[2]	252.0 0 (20)	252.07 (20)	4.40 (10)	4.43 (10)	172.00 (10)	171.74 (10)	2.00 (10)	2.09 (10)

[a]Non-self-consistent material constants as reported in the literature (uncertainties in last digits given in parentheses). Self-consistent material constants were fit from the same data with the third-order spatial equations used in the present study. [1]Data are from Sinogeikin and Bass (2000). [2]Data are from Li and Zhang (2005). $^{+}$Denotes non-self-consistent fit *Denotes self-consistent fit

To clarify that the distinction between self-consistent and non-self-consistent analyses does not affect our conclusions about spatial (Eulerian) *versus* material (Lagrangian) formulations, we obtained the self-consistent moduli for MgO by fitting the published experimental measurements using both formulations. We then extrapolated both fits to higher pressures using only the corresponding equations and compared with the data (Figure 12). We found that the spatial formulation remains better for both fitting and extrapolating data to higher pressures, as the elastic constants both derived and extrapolated self-consistently show larger misfits with respect to experimental data when based on the material rather than the spatial reference frame.

We performed the same test to compare thermodynamically self-consistent and non-self-consistent fits of the data for four materials (Figures 13–16). The results for MgO, $MgSiO_3$, and Ar are ambiguous, as both approaches provide comparably accurate extrapolations. However, the non-self-consistent approach fails in the comparison for H_2 (Figure 16), where it produces large misfits and, in the case of V_p and V_S, produces unrealistic curves that reverse direction. This is the only case—with non-self-consistent moduli—in which the spatial formulation fails, the result being to reinforce our finding that the self-consistent approach is preferable. Non-self-consistent fits to experimental measurements that have been published in the literature may therefore yield inaccurate values for the elastic moduli, so we refit the raw data using self-consistent equations and find that the values differ by up to ~3% from those reported in the literature (Table 6).

4. Conclusions

We have evaluated the reliability of spatial and material reference frames, as well as self-consistent and non-self-consistent approaches to deriving the finite-strain formulations for fitting the elastic moduli and sound velocities of materials under compression. We compare these formulations against data for nine materials having a wide range of elastic properties, highlighting the behavior of the shear modulus under compression. The comparisons show that the spatial (Eulerian) formulation reproduces experimental measurements more reliably than the material (Lagrangian) formulation and that self-consistently derived equations are at least, if not, more successful than non-self-consistently derived equations. Our results reinforce previous findings that had focused on the pressure-volume equation of state in showing that the shear properties are also best fit by a self-consistent finite-strain analysis based on the spatial frame of reference.

Acknowledgments
This work was supported by the U.S. Department of Energy, including under award DE-NA 0003842 and CDAC. We thank Lars Stixrude for helpful discussions and correspondence and the reviewers and editor for comments that helped us clarify our presentation. All data used in our analysis was produced by other authors. The data can be found in the following references: Ahart et al. (2011), Anderson and Swenson (1975), Boehler and Kennedy (1980), Brown (1999), Chen et al. (2010), Fei et al. (1993), Fiquet et al. (1998), Frankel et al. (1976), Goncharov et al. (2017), Grimsditch et al. (1986), Hemley et al. (1987), Ito et al. (1974), Jiang et al. (2009), Karki et al. (1997a&b), Kinoshita et al. (1979), Kuriakose et al. (2017), Li et al. (1996), Li and Zhang (2005), Marquardt et al. (2013), Murakami et al. (2009), Murakami et al. (2007), Packard and Swenson (1963), Polian and Grimsditch (1986), Ross et al. (1986), Sasaki et al. (2008), Shimizu et al. (1981), Shimizu et al. (1995), Shimizu et al. (2001), Sinogeikin and Bass (2000), Speziale et al. (2001), Suzuki (1975), Tange et al. (2012), Watanabe (1982), Whitfield et al. (1976), Zha et al. (1993), Zha et al. (2000), Zha et al. (2004), and Zha et al. (1998).

References

Ahart, M., Somayazulu, M., Gramsch, S. A., Boehler, R., Mao, H. K., & Hemley, R. J. (2011). Brillouin scattering of H2O ice to megabar pressures. *The Journal of chemical physics*, *134*(12), 124517. https://doi.org/10.1063/1.3557795

Anderson, M. S., & Swenson, C. A. (1975). Experimental equations of state for the rare gas solids. *Journal of Physics and Chemistry of solids*, *36*(3), 145–162.

Birch, F. (1947). Finite elastic strain of cubic crystals. *Physical review*, *71*(11), 809.

Birch, F. (1952). Elasticity and Constitution of the Earth's Interior. *Journal of Geophysical Research*, *57*(2), 227–286.

Birch, F. (1978). Finite Strain Isotherm and Velocities for Single-crystal and Polycrystalline NaCl at High Pressures and 300°K. *Journal of Geophysical Research*, *83*(B3), 1257–1268.

Boehler, R., & Kennedy, G. C. (1980). Equation of state of sodium chloride up to 32 kbar and 500 C. *Journal of Physics and Chemistry of Solids*, *41*(5), 517–523.

Brown, J. M. (1999). The NaCl pressure standard. *Journal of Applied Physics*, *86*(10), 5801–5808.

Chen, B., Gleason, A. E., Yan, J. Y., Koski, K. J., Clark, S., & Jeanloz, R. (2010). Elasticity, strength, and refractive index of argon at high pressures. *Physical Review B*, *81*(14), 144110.

Davies, G. F. (1973a). Quasi-harmonic finite strain equations of state of solids. *Journal of Physics and Chemistry of Solids*, *76*, 7.

Davies, G. F. (1973b). Invariant finite strain measures in elasticity and lattice dynamics. *Journal of Physics and Chemistry of Solids*, *34*(5), 841–845.

Davies, G. F. (1974). Effective elastic moduli under hydrostatic stress—I. quasi-harmonic theory. *Journal of Physics and Chemistry of Solids*, *35*(11), 1513–1520.
Davies, G. F., & Dziewonski, A. M. (1975). Homogeneity and constitution of the Earth's lower mantle and outer core. *Physics of the Earth and Planetary Interiors*, *10*(4), 336–343.
Fei, Y., Mao, H. K., & Hemley, R. J. (1993). Thermal expansivity, bulk modulus, and melting curve of H_2O–ice VII to 20 GPa. *The Journal of Chemical Physics*, *99*(7), 5369–5373.
Fiquet, G., Andrault, D., Dewaele, A., Charpin, T., Kunz, M., & Haüsermann, D. (1998). PVT equation of state of $MgSiO_3$ perovskite. *Physics of the Earth and Planetary Interiors*, *105*(1), 21–32.
Frankel, J., Rich, F. J., & Homan, C. G. (1976). Acoustic velocities in polycrystalline NaCl at 300 K measured at static pressures from 25 to 270 kbar. *Journal of Geophysical Research*, *81*(35), 6357–6363.
Grimsditch, M., Loubeyre, P., & Polian, A. (1986). Brillouin scattering and three-body forces in argon at high pressures. *Physical Review B*, *33*(10), 7192.
Hemley, R. J., Jephcoat, A. P., Mao, H. K., Zha, C. S., Finger, L. W., & Cox, D. E. (1987). Static compression of H_2O-ice to 128 GPa (1.28 Mbar). *Nature*, *330*(6150), 737.
Hill, R. (1952). The elastic behaviour of a crystalline aggregate. *Proceedings of the Physical Society of London Section A*, *65*, 349–355.
Ito, H., Kawada, K., & Akimoto, S. I. (1974). Thermal expansion of stishovite. *Physics of the Earth and Planetary Interiors*, *8*(3), 277–281.
Jackson, I. (1998). Elasticity, composition and temperature of the Earth's lower mantle: a reappraisal. *Geophysical Journal International*, *134*(1), 291–311.
Jeanloz, R. (1989). Shock wave equation of state and finite strain theory. *Journal of Geophysical Research*, *94*(B5), 5873–5886.
Jiang, F., Gwanmesia, G. D., Dyuzheva, T. I., & Duffy, T. S. (2009). Elasticity of stishovite and acoustic mode softening under high pressure by Brillouin scattering. *Physics of the Earth and Planetary Interiors*, *172*(3-4), 235–240.
Karki, B. B., Stixrude, L., Clark, S. J., Warren, M. C., Ackland, G. J., & Crain, J. (1997a). Structure and elasticity of MgO at high pressure. *American Mineralogist*, *82*(1-2), 51–60.
Karki, B. B., Stixrude, L., Clark, S. J., Warren, M. C., Ackland, G. J., & Crain, J. (1997b). Elastic properties of orthorhombic $MgSiO_3$ perovskite at lower mantle pressures. *American Mineralogist*, *82*(5), 635–638.
Kinoshita, H., Hamaya, N., & Fujisawa, H. (1979). Elastic properties of single-crystal NaCl under high pressures to 80 kbar. *Journal of Physics of the Earth*, *27*(4), 337–350.
Kuriakose, M., Raetz, S., Hu, Q. M., Nikitin, S. M., Chigarev, N., Tournat, V., et al. (2017). Longitudinal sound velocities, elastic anisotropy, and phase transition of high-pressure cubic H_2O ice to 82 GPa. *Physical Review B*, *96*(13), 134122.
Latimer, K., Dwaraknath, S., Mathew, K., Winston, D., & Persson, K. A. (2018). Evaluation of thermodynamic equations of state across chemistry and structure in the materials project. *npj Computational Materials*, *4*(1), 40.
Li, B., Rigden, S. M., & Liebermann, R. C. (1996). Elasticity of stishovite at high pressure. *Physics of the Earth and Planetary Interiors*, *96*(2-3), 113–127.
Li, B., & Zhang, J. (2005). Pressure and temperature dependence of elastic wave velocity of $MgSiO_3$ perovskite and the composition of the lower mantle. *Physics of the Earth and Planetary Interiors*, *151*(1-2), 143–154.
Marquardt, H., Speziale, S., Gleason, A., Sinogeikin, S., Kantor, I., & Prakapenka, V. B. (2013). Brillouin scattering and x-ray diffraction of solid argon to 65 GPa and 700 K: Shear strength of argon at HP/HT. *Journal of Applied Physics*, *114*(9), 093517.
Marquardt, H., Speziale, S., Reichmann, H. J., Frost, D. J., & Schilling, F. R. (2009). Single-crystal elasticity of (Mg0. 9Fe0. 1) O to 81 GPa. *Earth and Planetary Science Letters*, *287*(3-4), 345–352.
Murakami, M., Ohishi, Y., Hirao, N., & Hirose, K. (2009). Elasticity of MgO to 130 GPa: Implications for lower mantle mineralogy. *Earth and Planetary Science Letters*, *277*(1-2), 123–129.
Murakami, M., Sinogeikin, S. V., Hellwig, H., Bass, J. D., & Li, J. (2007). Sound velocity of $MgSiO_3$ perovskite to Mbar pressure. *Earth and Planetary Science Letters*, *256*(1-2), 47–54.
Murnaghan, F. D. (1937). Finite deformations of an elastic solid. *American Journal of Mathematics*, *59*(2), 235–260.
Packard, J. R., & Swenson, C. A. (1963). An experimental equation of state for solid xenon. *Journal of Physics and Chemistry of Solids*, *24*(12), 1405–1418.
Polian, A., & Grimsditch, M. (1986). Elastic properties and density of helium up to 20 GPa. *EPL (Europhysics Letters)*, *2*(11), 849.
Ross, M., Mao, H. K., Bell, P. M., & Xu, J. A. (1986). The equation of state of dense argon: A comparison of shock and static studies. *The Journal of chemical physics*, *85*(2), 1028–1033.
Sasaki, S., Wada, N., Kume, T., & Shimizu, H. (2008). High-pressure Brillouin study of the elastic properties of rare-gas solid xenon at pressures up to 45 GPa. *Journal of Raman Spectroscopy: An International Journal for Original Work in all Aspects of Raman Spectroscopy, Including Higher Order Processes, and also Brillouin and Rayleigh Scattering*, *40*(2), 121–127.
Shimizu, H., Brody, E. M., Mao, H. K., & Bell, P. M. (1981). Brillouin Measurements of Solid n-H 2 and n-D 2 to 200 kbar at Room Temperature. *Physical Review Letters*, *47*(2), 128.
Shimizu, H., Nabetani, T., Nishiba, T., & Sasaki, S. (1995). High-pressure elastic properties of the VI and VII phase of ice in dense H_2O and D_2O. *Physical Review B*, *53*(10), 6107.
Shimizu, H., Tashiro, H., Kume, T., & Sasaki, S. (2001). High-pressure elastic properties of solid argon to 70 GPa. *Physical review letters*, *86*(20), 4568–4571. https://doi.org/10.1103/PhysRevLett.86.4568
Sinogeikin, S. V., & Bass, J. D. (2000). Single-crystal elasticity of pyrope and MgO to 20 GPa by Brillouin scattering in the diamond cell. *Physics of the Earth and Planetary Interiors*, *120*(1-2), 43–62.
Speziale, S., Zha, C. S., Duffy, T. S., Hemley, R. J., & Mao, H. K. (2001). Quasi-hydrostatic compression of magnesium oxide to 52 GPa: Implications for the pressure-volume-temperature equation of state. *Journal of Geophysical Research*, *106*(B1), 515–528.
Stixrude, L., & Lithgow-Bertelloni, C. (2005). Thermodynamics of mantle minerals—I. Physical properties. *Geophysical Journal International*, *162*(2), 610–632.
Stixrude, L., & Lithgow-Bertelloni, C. (2010). Thermodynamics of the Earth's mantle. *Reviews in Mineralogy and Geochemistry*, *71*(1), 465–484.
Suzuki, I. (1975). Thermal expansion of periclase and olivine, and their anharmonic properties. *Journal of Physics of the Earth*, *23*(2), 145–159.
Tange, Y., Kuwayama, Y., Irifune, T., Funakoshi, K. I., & Ohishi, Y. (2012). P-V-T equation of state of $MgSiO_3$ perovskite based on the MgO pressure scale: A comprehensive reference for mineralogy of the lower mantle. *Journal of Geophysical Research*, *117*, B06201. https://doi.org/10.1029/2011JB008988
Thomsen, L. (1972). The fourth-order anharmonic theory: elasticity and stability. *Journal of Physics and Chemistry of Solids*, *33*(2), 363–378.

Thurston, R. N. (1965). Effective elastic coefficients for wave propagation in crystals under stress. *The Journal of the Acoustical Society of America*, *37*(2), 348–356.
Wallace, D. C. (1972). *Thermodynamics of Crystals*. Mineola, NY: Dover Publications.
Watanabe, H. (1982). Thermochemical properties of synthetic high-pressure compounds relevant to the Earth's mantle. *Hith-Pressure Research in Geophysics*, 441–464.
Weiner, J. H. (2002). *Statistical Mechanics of Elasticity*. Mineola, NY: Dover Publications.
Whitfield, C. H., Brody, E. M., & Bassett, W. A. (1976). Elastic moduli of NaCl by Brillouin scattering at high pressure in a diamond anvil cell. *Review of Scientific Instruments*, *47*(8), 942–947.
Zha, C. S., Duffy, T. S., Mao, H. K., & Hemley, R. J. (1993). Elasticity of hydrogen to 24 GPa from single-crystal Brillouin scattering and synchrotron x-ray diffraction. *Physical Review B*, *48*(13), 9246.
Zha, C. S., Mao, H. K., & Hemley, R. J. (2000). Elasticity of MgO and a primary pressure scale to 55 GPa. *Proceedings of the National Academy of Sciences*, *97*(25), 13,494–13,499.
Zha, C. S., Mao, H. K., & Hemley, R. J. (2004). Elasticity of dense helium. *Physical Review B*, *70*(17), 174107.
Zha, C. S., Mao, H. K., Hemley, R. J., & Duffy, T. S. (1998). Recent progress in high-pressure Brillouin scattering: olivine and ice. *The Review of High Pressure Science and Technology*, *7*, 739–741.